İSTANBUL TECHNICAL UNIVERSITY ★ INSTITUTE OF SCIENCE AND TECHNOLOGY

WAKE STRUCTURE OF A THREE DIMENSIONAL CAR MODEL EXPOSED TO CROSSWIND

M.Sc. Thesis by
Esra ÖZDEMİR, B.A. Chem.
514981006

Date of submission : **6 November 2001**

Date of defense examination : **27 November 2001**

Supervisor (Chairman) : **Prof. Dr. İ. Bedii ÖZDEMİR**

Members of the Examining Committee : **Prof. Dr. Ali GÖKTAN (İ.T.Ü.)**

Prof. Dr. Ertuğrul ASLAN (İ.T.Ü.)

NOVEMBER 2001

İSTANBUL TEKNİK ÜNİVERSİTESİ ★ FEN BİLİMLERİ ENSTİTÜSÜ

ÇAPRAZ RÜZGARA MARUZ KALMIŞ ÜÇ BOYUTLU TAŞIT MODELİNDE ARDİZ YAPILARI

YÜKSEK LİSANS TEZİ

Kimyager Esra ÖZDEMİR
514981006

Tezin Enstitüye Verildiği Tarih : 6 Kasım 2001

Tezin Savunulduğu Tarih : 27 Kasım 2001

Tez Danışmanı : Prof. Dr. İ. Bedii ÖZDEMİR

Diğer Jüri Üyeleri : Prof. Dr. Ali GÖKTAN (İ.T.Ü.)

Prof. Dr. Ertuğrul ASLAN (İ.T.Ü.)

KASIM 2001

ACKNOWLEDGMENT

The author is pleased to acknowledge the guidance and inspiration provided by her supervisor, Prof. Dr. İ. Bedii Özdemir, in the research program for this thesis. Professor Özdemir's encouraging attitude and continuous interest in the work led the author to the completion of this thesis.

It has been a pleasure to work with many research students, and to benefit from their advice and good friendship. The author's association with Mr. G. Özkan, Mr. Ö. Dölek and E. O. Kozaka has been particularly valuable.

For financial support during the work, the author is indebted to TÜBİTAK for the studentship provided under the grant MİSAG 163. In addition, the support by TOFAŞ A.Ş., which provided the replicated model car, was greatly appreciated.

The author also extends her deepest gratitude to her mother in law Meral Özdemir for taking care of her beloved son Recep İlteber Özdemir throughout her M.Sc. study.

November 2001

Esra Özdemir

B.A. Chemistry

CONTENTS

LIST OF FIGURES

LIST OF TABLES

LIST OF SYMBOLS

A_1	Area of the measurement plane (0.24×0.33 m^2)
c	Speed of sound
C_w	Heat capacity of wire
d_w	Wire diameter
e	Thermal energy
E	Output voltage of the wire
E_{acq}	Voltage acquired
E_{corr}	Corrected output voltage
F_x	Momentum deficit in the x-direction
F_y	Momentum deficit in the y-direction
F_z	Momentum deficit in the z-direction
g	Gravitational acceleration
Gr	Grashoff number, $g\beta d_w^3 (T_w - T_a)/\upsilon^2$
h	Convective coefficient of heat transfer
H	Joule heating of the wire
k_f	Conductive coefficient of fluid
k_w	Conductive coefficient of wire
I	Wire current
l_w	Length of the wire
Ma	Mach number, U/c
Nu	Nusselt number, $\mathrm{Nu} = hd_w / k_f$
P	Static pressure
Pr	Prandtl number, α/υ
Q	Heat transfer to surroundings
Q_{conv}	Convective heat transfer to fluid
Q_{cond}	Conductive heat transfer to wire supports
Q_{rad}	Radiation heat transfer to surroundings
R_w	Wire resistance
Re_c	Reynolds number, $U_c L_F/\upsilon$
Re_∞	Reynolds number, $W_\infty L_F/\upsilon$
t	Time
T_a	Ambient temperature
T_{ref}	Reference temperature
T_s	Wire support temperature
T_w	Wire temperature
u	Lateral turbulent velocity
$\sqrt{\overline{u^2}}$	Lateral fluctuation velocity (root mean square, rms)
U	Lateral velocity
$\overline{U}$	Lateral mean velocity

U_c	Crosswind velocity
v	Transversal turbulent velocity
$\sqrt{\overline{v^2}}$	Transversal fluctuation velocity (root mean square, rms)
V	Transversal velocity
$\overline{V}$	Transversal mean velocity
w	Streamwise turbulent velocity
$\sqrt{\overline{w^2}}$	Streamwise fluctuation velocity (root mean square, rms)
W	Streamwise velocity
$\overline{W}$	Streamwise mean velocity
W_∞	Approach velocity
x	Lateral distance
Δx	Grid size in the x-direction (1 cm)
y	Transversal distance
Δy	Grid size in the y-direction (1 cm)
z	Streamwise distance
α	Yaw angle
β	Thermal coefficient of expansion
υ	Kinematic viscosity of air
ρ	Density of the air
ζ_0	Contour of zero $\overline{U}$ velocity

WAKE STRUCTURE OF A THREE DIMENSIONAL CAR MODEL EXPOSED TO CROSSWIND

SUMMARY

The aerodynamic aspects of turbulent drag induced by a crosswind have been studied behind a scaled model car. For this purpose, full kinematic map of the wake, including time-averaged structures of the turbulent flow were examined by local measurements of velocity on a plane at a distance half the square root frontal area downstream of the model, exposed to approach velocities 18, 28 and 38 m/s and crosswind speeds of 3.2, 4.9 and 6.7 m/s.

The vector map of in-plane velocities have shown two counter-rotating vortices located asymmetrically on both side of the center plane of the model. These vortices play an important role in the production and transport of turbulent kinetic energy and seem to be less affected by changes in the approach velocity. In the course of turbulent energy exchange, the vortices act like a system putting the energy from the crosswind back into the mean flow. The vortex centers can be envisaged as the manifolds leaking the turbulent energy out of the plane motion, which was extracted from the crosswind flow via processes leading to the vortex formation in the core of the wake. The overall process resulted in the turbulence generated by the crosswind being less effective in producing additional drag.

Calculations of streamwise momentum deficits based on time-averaged mean velocities also reveal that increasing the approach velocity leads to decrease in dynamic forces applied, including the lateral force induced by crosswind.

Key Words: Car Aerodynamics, Fluid Mechanics, Measurements.

ÇAPRAZ RÜZGARA MARUZ KALMIŞ ÜÇ BOYUTLU TAŞIT MODELİNDE ARDİZ YAPILARI

ÖZET

Çapraz rüzgar tarafından oluşturulan çalkantıya bağlı gelişen sürüklenmenin özellikleri ölçeklenmiş model araç arkasındaki akış ile aerodinamik açıdan çalışılmıştır. Zaman-ortalaması alınmış çalkantı yapıları modelden yarım tipik uzaklıktaki bir düzlemde yapılan yerel hız ölçümleri ile incelenmiştir. Deneyler modelin önden 18, 28, 38 m/s lik hızlarda akışa maruz kalırken yandan 3.2, 4.9, and 6.7 m/s lik çapraz rüzgar aldığı durumlarda yapılmıştır.

Hız alanının ölçüm düzlemi üzerindeki izdüşümü, aracın merkez ekseninin her iki yanında asimetrik olarak birbirine ters yönde dönen girdap yapılarını ortaya koymaktadır. Bu yapıların çalkantı üretme ve taşıma konusunda oldukça etkin bir rol üstlendikleri ve bu durumun önden gelen akış hızından bağımsız kaldığı görülmüştür. Çalkantı kinetik enerjisinin düzlem içi ve düzlem dışı yapılarla alış verişi incelendiğinde, bu döngüsel yapıların çapraz rüzgardan alınan enerjiyi ortalama hız alanına geri kazandıran bir sistem gibi algılanması olanaklı gözükmektedir. Öyle ki, döngünün oluşması sırasında yaratılan çalkantı enerjisinin yine bu döngü merkezlerinden düzlem dışına çıktığı anlaşılmaktadır. Bütün bu süreç sonucunda çapraz rüzgar tarafından oluşturulan çalkantının sürüklenme kuvveti yaratmada pek de etkili olmadığı sonucunu doğurmaktadır.

Eğer ortalama hızlara dayanılarak akış yönünde oluşan momentum eksikliği hesaplanırsa, önden gelen hızların artışına rağmen, dinamik kuvvetlerin azaldığı görülmektedir ki, bu da yukarıda sözü edilen süreci doğrular niteliktedir.

Anahtar Kelimeler: Taşıt Aerodinamiği, Akışkanlar Mekaniği, Ölçme.

1. INTRODUCTION

1.1. Research Rationale

The handling characteristics, stability and fuel economy of passenger vehicles are known greatly influenced by aerodynamic properties. In recent years, trends for lighter vehicles to reduce fuel consumption have, yet, resulted in vehicles becoming more susceptible to any aerodynamic forcing due to oscillations of the vehicle wake (Sims-Williams and Dominy 1998). Because of this, there is now an increased interest in the prediction of the dynamic stability of a vehicle in particular in crosswind conditions (Dominy 1991).

1.2. Cross-Wind Effects

The natural wind has an almost continuous influence on the handling characteristics of all road vehicles. This may be negligible at low wind speeds but as both vehicle and wind speeds increase the ride is degraded, leading ultimately to a safety problem. For low crosswind conditions, the primary concern is vehicle stability, which includes vehicle displacement spectrum in a turbulent cross flow (Ryan and Dominy 1997). For such an analysis, the basic aerodynamic data required is knowledge of the vehicle force and moment coefficients at low yaw angles and of the development of these forces on entry to a gust (Ryan and Dominy 1998, Dominy and Ryan 1999). For high cross flow conditions, vehicle safety is usually the main problem, i.e., the avoidance of overturning or sideslip accidents. This requires knowledge of the aerodynamic force and moment coefficients at high yaw angles that are relevant to extreme crosswind conditions (Cigada *et al.* 2001).

The principal vehicle characteristic, which has influence on crosswind sensitivity, is the yaw rate response to a given wind input which, as with any aerodynamic parameter, is strongly dependent on vehicle shape. Experiments (Howell 1996) show that the side force coefficient for a particular vehicle seems to be remarkably insensitive to Reynolds number. However, for the mean lift force coefficients there is much greater variation with a pronounced Reynolds number effect, particularly at the higher yaw angles. For both side and lift force coefficients the extreme/mean ratios are found significantly above 1.0 for the low and high yaw angle ranges and close to 1.0 in the mid yaw angle range. The low yaw angle behaviour was attributed to low mean coefficient values, whilst the high yaw angle behaviour was attributed to body induced unsteadiness, i.e. vortex shedding (Dominy 1995).

As the low-frequency oscillation of the vehicle wake can affect the stability of the vehicle, a more detailed understanding of the oscillatory nature of a wake (Ahmed 1981) is necessary if appropriate design decisions are to be made. Unfortunately, previous works (Buchheim *et al.* 1987) have often assumed that the flow in the wake behind a vehicle is steady or quasi-steady. It is from this assumption that the traditional picture of a vehicle wake with two counter-rotating vortices emerges. In reality, however, the wake is seen to have large time-dependent component demonstrating that the idealized model of two vortices that are steady in time is not true. Recent studies (Himeno and Fujitani 1993, Angelis *et al.* 1996) have confirmed this by showing large-scale vortical structures distributed throughout the wake that not only move with time but also created and destroyed as time evolves.

The aim of this thesis is, therefore, to document the structure of the separated flow behind a replicated scale model in crosswind conditions in sufficient detail to develop a strategy to determine the effects of the upstream flow and model geometry on the flow within the shear layer and in the separated region below the shear layer. Next, background information on wake flows is given.

1.3. Generic Structure of the Wake Flows

Turbulent flow past bluff bodies (Bearman 1997) forms on important class of flow problems which has many practical applications ranging from wind engineering to aerodynamics of road vehicles as mentioned above. Therefore, there has been a strong impetus over the last decade to understand vortex dynamics in wake flows (Williamson 1997), which are important not only for our understanding of fundamental flow physics, but also for the many applications of bluff body flows in technology. A particular emphasis of the recent surge of activity concerns three-dimensional aspects of wake flows behind bodies exposed to strong cross flow (Hangan and Vickery 1997). Such effects are important when one considers the integrated unsteady forces on a vehicle, especially in the context of vortex-induced vibrations in crosswind conditions. However, numerical simulation for this class of problems becomes difficult due to the geometry of the body and the lack of ability of the standard turbulence models to simulate the complex turbulent structure that exists inside the body wake (Han 1989, Huan and Lin 2000).

An important feature of a bluff body is that very strong interactions take place between viscous and inviscid regions of its flow field. The flow over bluff bodies generally develops attached, but the adverse pressure gradient that this flow imposes on the boundary layer will soon becomes too great to sustain the attachment. Usually, bluff bodies induce flow separation at positions where the velocity at the edge of the boundary layer is higher than the free stream velocity. This results in a high rate of shedding of circulation which in turn leads to a high time-mean drag which is experienced primarily as a difference in pressure between the windward and leeward faces on the body.

Flow separation from bluff bodies may occur either from sharp edges or from continuous surfaces. The prediction of separation position from a continuous surface is particularly difficult because it depends on both the characteristics of the upstream boundary layer and the structure of the region of flow just downstream of the body known as the near wake (Parameswaran *et al.* 1997). The flow domain immediately downstream of a bluff body contains reversed flow and is bounded by free shear layers. Within this region, various forms of flow instability may be initiated and amplified. Furthermore as an added complication for a bluff body the boundary layer, separation position may oscillate in response to pressure gradients imposed by unsteady flow features in the near wake. It is due to the generation and shedding of the coherent vortices, that large unsteady force may develop, particularly in a direction transverse to that of the main flow. In addition, in almost all instances the maximum design pressure occurs in regions of separated flow. Therefore, the flow in the near wake region behind a bluff body plays an important role in determining the steady and unsteady forces acting on the body. The details of the flow in these separated regions and the criteria for physical modeling of the flows in these regions are not well understood. Any new insights into the mechanism of fluid structure interaction in a turbulent flow must come from a better understanding of the details of the separated flow, the properties of the separated shear layers and the flow in the regions between these shear layers and the bluff body.

It is a widely held view that provided that the separation point is predetermined by geometry, all essential relations in the flow are rather independent of Reynolds number and, hence, that tests on small scale models are an acceptable method for obtaining information which can be applied to full scale models. Recent studies on bluff body aerodynamics, however, show that the separated flow at the windward side of the models is Reynolds number dependent (Hoxey *et al.* 1998). Corroborating evidence was obtained by changing the conventional sharp line edges in full and model scale experiments, which produced predominately attached flow, for which no Reynolds number sensitivity was observed. It is, then, proposed that the observed Reynolds number sensitivity can be attributed to the formation and subsequent instability of the vortex sheet formed from vortices generated at the edges. The Reynolds number sensitivity in bluff body aerodynamics can, thus, be explained by considering the motion of a vortex pair, which indicates a Reynolds number dependency particularly in the vicinity of reattachment. Experimental observations (Akins and Reinhold 1998) show that vortices generated at the frontal edges initially separate from the upper surface as they are transported downstream before eventually reattaching and recirculating. The shape of the leading edge of the bubble is stationary and Reynolds number independent, whereas the trailing edge seems to be transient, that is, the location of the reattachment point fluctuates, in time, about its mean position and is Reynolds number dependent. This particular form of transience is intrinsic to the dynamics of the vortices and results from turbulent velocity fluctuations and fluctuations in the mean speed and its direction. The average location of the reattachment point as well as the height of the separation bubble were found to scale with the inverse of Reynolds number as 1/Re and, thus intriguingly, the length-to-height ratio of the separation bubble is expected to be Reynolds number independent.

As a final remark, it should be pointed out that the structure of the bluff body wake consists of two regions, an internal wake region where a deficit turbulence mechanism (similar to the deficit velocity and hence of Gaussian type) can be assumed, and an external wake region where dissipation laws are dominant. There is a strong evidence that the coherent structure (vortex) in turbulent flow dies faster than in smooth flow and it is probable that for a smaller scale turbulent flow this fact would be more evident.

1.4. Methodology

Flow over road vehicles is complex and difficult to predict with accuracy. Designers will therefore continue to rely on wind tunnel testing in efforts to produce low-drag designs. The aerodynamic characteristics as response of a car to windy conditions are also conventionally determined from steady-state wind tunnel tests (Baker and Humphreys 1996). It is usual to measure the overall forces and moments acting on the vehicle in a yawed condition, which simulates a superimposed natural wind input. While this provides an important global view of the lateral aerodynamics, i.e., side force, yawing moment and center of pressure, it does not provide information on unsteadiness due to wake of the car. A full kinematical map of the body wake can only generate this information with momentum loads being obtained from an integration of the dynamic pressures acting over a defined area.

Since small design details can often have a substantial influence on aerodynamic properties, testing of full-scale models is desirable. However, because this cannot be physically possible for most of the cases or be costly, one has to conduct experiments on scaled models. One of the several sources of inaccuracy in the interpretation of wind tunnel data is the constraint imposed by wind tunnel walls on the flow around the model. The ratio of model size to wind tunnel test section size is called blockage ratio and is limited by the wall interference effects. The most prominent symptom of the blockage interference is an increase of velocity over the model if the walls are closed, or a decrease of velocity if the tunnel boundaries are fully open. The calculations, validated by comparisons with measured car surface and wind tunnel wall pressures, show that the drag coefficient requires a negative correction if measured in a closed test section and a positive correction if measured in an open test section (Mokry 1995). In addition, the streamwise variation of the wall induced pressure gives rise to buoyancy drag. The blockage corrections are also somewhat dependent on the axial position of the model in the test section and its conditions. Therefore, wind tunnel experiments should be designed to minimize interference effects. Wind tunnels with adjustable test sections (Kong and Parkinson 1995) have some excellent characteristics in this respect. Experiments in partially open test sections (Broughton *et al.* 1995) show that blockage corrections are much smaller than for solid wall test sections and that for 30% open area ratio (OAR), the measurement was practically interference-free up to blockage ratios of about 15%. It has been argued that a model with 28.5% blockage and a length about half that of the test section can be tested in a ring-airfoil configuration with OAR just under 50% and give a drag coefficient requiring no blockage correction. Furthermore, side force and rolling moment data, which are virtually interference-free, can be attained for models with blockage up to 15% in test sections with OAR of 30%. The test-section configuration has a major effect not only on the loading on the model but also on the nature of the flow pattern about it. It has been shown that as OAR is increased from zero, the stagnation region on the front surface of the model is moved upward and the local positive pressures are decreased until in the open jet configuration the flow is seen completely separated over the front surface.

The re-entry of flow from the plenum into the wind tunnel circuit at the downstream end of the test section also have an important influence on pressure distribution over the downstream portion of the model. Adjustable re-entry flaps to vary collector area (Wolf 1995) are an effective means of controlling the re-entry flow and the wake pressure at the downstream boundary conditions to be established. On the open jet performance of wind tunnels, however, it has been seen that the collector has no effect.

The blockage characteristics in an experiment are also dependent on model shape. Experiments on simple shapes have shown that the data for the sharp block were subject to substantial interference effects even for much lower values of blockage ratio, from which both wall constraint and test-section exit proximity effects appear to be responsible. On the other hand, wall constraint effects were small, at least in absolute terms, for the rounded blocks. This indicates that body shapes having a separation and reattachment, i.e., a closed separation bubble, on their lateral surfaces are particularly prone to wall constraint effects.

In automotive wind tunnel testing, the thickness of the ground plane boundary layer in the flow approaching the models is determined by factors other than the model size and geometry. Consequently, the boundary layer thickness does not scale when the model size is altered, which constitutes a source of dissimilarity or interference, which needs to be eliminated (Parameswaran *et al.* 1993). Although it is often assumed that the typical flow fields and ground clearance involved in commercial vehicle configurations do not require the simulation of vehicle-ground interface, recent concern about the influence of using fixed or rotating wheels on scale models has led to interest in the mechanism which governs underbody and base flow fields. A number of different techniques are available to simulate the vehicle-ground interface when using a stationary model in a wind tunnel. Amongst the most common is moving ground plane. This technique involves the removal of the wind tunnel wall boundary layer upstream of an endless moving belt surface, the movement of which serves to prevent the boundary layer developing in the vicinity of the model. Particularly revealing parameter for this phenomenon is the base pressure coefficient (base suction), which, in contrast to some of the other parameters of the flow, responds sensitively to the changes in flow stability throughout a wide range of Reynolds numbers. Experiments on rectangular block models (Garry 1996) show some dependence of base pressure on the forebody flow field, in that at small ground clearance the increase in base pressure for a streamlined model is slightly less than that for the model with separated leading edge flow. It was argued that on single models reducing the relative moving ground/air speed results in an increase in the floor boundary layer displacement thickness, which appears physically similar to that of reducing the model ground clearance.

2. EXPERIMENTAL TECHNIQUES

2.1. Flow Configuration

The experiments were conducted in an open circuit subsonic wind tunnel, ANKA, (figure 2.1) which was comprised of a centrifugal fan, an inlet diffuser, a settling chamber, a well-defined contraction and a straight-ducted test section with an exhaust duct and exit diffuser. The blower was fixed on shock absorbers and connected to the rest of the tunnel installation with a flexible coupling to avoid transmittance of vibration and a possible resonance. Air streams from the blower expanded through a screen of mesh size 4 mm^2 and an inlet diffuser which was placed between the blower exit and the settling chamber to reduce the flow speed and thus to increase pressure. The settling chamber was 1000 mm in length and of 1400×1400 mm^2 in cross-section and, consisted of three mesh screens to damp out flow irregularities and to develop a low-turbulence uniform flow before the test section. Of these, the first two were 4 mm^2 in size and separated at an interval of 250 mm, and the last one with finer size of 0.25 mm^2 was placed at a distance of 500 mm downstream. The contraction was placed just before the test section to reduce variations of the mean velocity and fluctuations to negligibly small values. The test section was 500×500 mm^2 in cross-section and 3920 mm in length with upper and side walls made of Plexiglas to allow light transmittance.

2.2. The Model

The experiments were performed on a replicated 1:8 scale model of Fiat Brava 16V, a hatchback car with a 1.6 liter engine. The model body was manufactured from Styrofoam molding covered with polyester with a tolerance error of less than 1.2% and the external surfaces were fine finished and polished. The principal dimensions of the car and the replicated model were given in table 2.1. The model had a frontal projection area of 27,614 mm^2, which resulted in a blockage ratio of 11% in the test

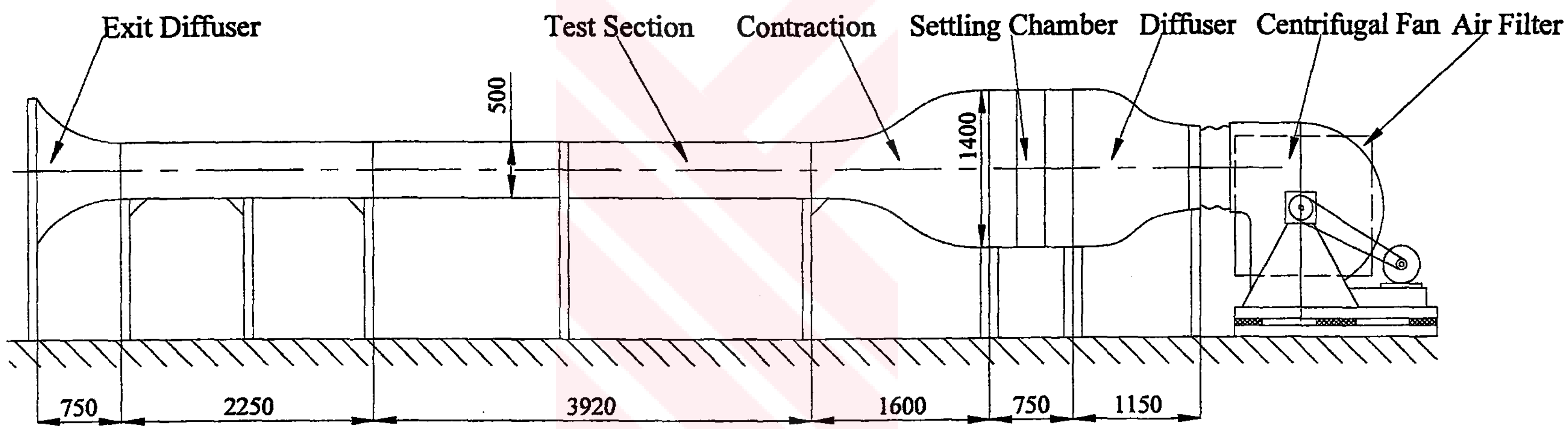

Figure 2.1 Schematic of the ANKA wind tunnel

Table 2.1. Full scale and model dimensions

Principle Dimensions (cm)	**Full Size Vehicle**	**Replicated 1:8 Scale Model**
Length	418.7	51.8
Width (excluding mirrors)	174.1	21.8
Height	140.8	17.6

section. The side projection area of the model was 56,225 mm^2. The typical length scales based on the square root of the projected frontal and lateral areas were 166 and 237 mm, respectively.

The model rest on its wheels on a mounting pad made of a steel plate of 4 mm in thickness and 350×600 mm^2 in cross-section (figure 2.2). The pad was extended

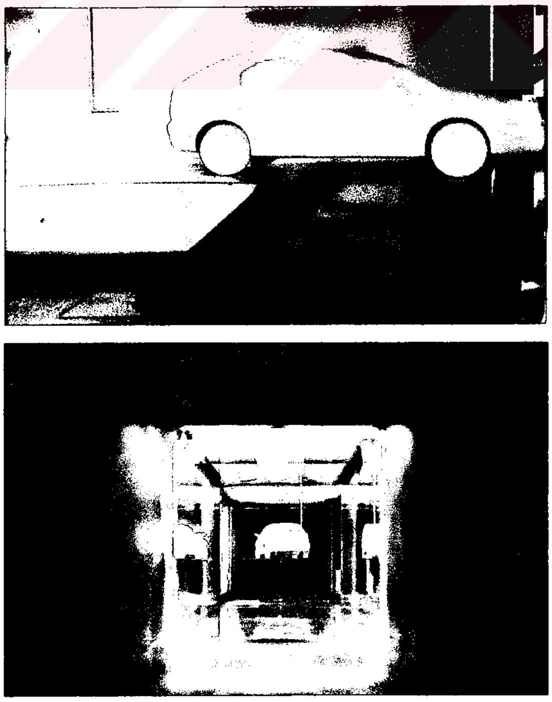

Figure 2.2 The model and mounting pad

from 30 mm inside the leading point of the model to a distance of 113 mm downstream. With this configuration, the model was exposed to a uniform freestream at the front while the ground effect was still simulated in its wake with conditions imposed by the extending solid wall. The pad was held 250 mm above the tunnel floor with a strut plate of 5 mm thickness and 40 mm width, which was inclined upstream at 40 degrees and intersected the pad at 100 mm inside the leading edge. The edges of the pad and the strut were all sharpened, and welded junctions were smoothly rounded so to avoid any disturbance and flow separation under the model. The pad assembly was placed with front edge at 240 mm downstream of the entrance of the test section, which resulted in the downstream face of the model located 500 mm upstream test-section exit to avoid incorrect static pressure at test-section exit due to wake blockage at the collector.

The crosswind effect was produced by giving the model a yaw angle of 10 degrees. By adjusting the tunnel speed, this provided various crosswind speeds (U_c) with the corresponding vehicle speeds (W_∞) (from now on it will be called the approach velocity) given in table 2.2.

Table 2.2. The approach and crosswind velocities

Tunnel Speed (m/s)	W_∞ (m/s)	Re_∞	U_c (m/s)	Re_c
18.28	18	0.20×10^6	3.2	0.50×10^5
28.43	28	0.31×10^6	4.9	0.78×10^5
38.59	38	0.42×10^6	6.7	1.06×10^5

2.3. Velocity Measurements

2.3.1. Principle of Operation of Hot-Wire Anemometer

The hot-wire anemometer was the most suitable instrument to measure mean and fluctuating variables in the flow described in this thesis. The anemometer provided an analogue output, which represented the velocity at a point in the flow field. In order to understand its principle of operation, consider a thin wire stretched between two supports and exposed to a velocity U (figure 2.3). When a current is passed through wire, heat is generated at a rate $I^2 R_w$ and, in equilibrium; this must be balanced by heat loss (primarily convective) to the surroundings. If velocity changes, convective heat transfer coefficient and so the wire temperature will change and eventually reach a new equilibrium.

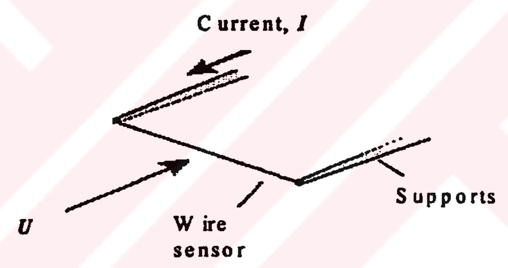

Figure 2.3 Schematic of hot-wire

The governing equation can be written as

$$\frac{\mathrm{d}e}{\mathrm{d}t} = H - Q \tag{2.1}$$

where $e = C_w T_w$ is the thermal energy stored in the wire, $H = I^2 R_w$ power generated by Joule heating and Q is the heat transferred to surroundings which includes convection to fluid,

$$Q_{conv} = hA\left(T_w - T_a\right), \tag{2.2}$$

conduction to supports

$$Q_{cond} = f(T_w, l_w, k_w, T_s), \tag{2.3}$$

and radiation to surroundings

$$Q_{rad} = f(T_w^4 - T_a^4). \tag{2.4}$$

Nusselt number is defined as

$$\mathrm{Nu} = \frac{hd_w}{k_f} = f(\mathrm{Re}, \mathrm{Pr}, \mathrm{Ma}, \mathrm{Gr}) \tag{2.5}$$

and is, in general, a function of Reynolds number $\mathrm{Re} = Ud_w/\upsilon$, Prandtl number $\mathrm{Pr} = \alpha/\upsilon$, Mach number $\mathrm{Ma} = U/c$, and Grashoff number $\mathrm{Gr} = g\beta d_w^3 (T_w - T_a)/\upsilon^2$, where h is convective coefficient of heat transfer, A is the heat transfer area, d_w is the wire diameter, C_w is the heat capacity of wire and k_f is the heat conductivity of the fluid. Assuming that radiation losses and conduction to wire supports are small, T_w is uniform over the length of the sensor and velocity is uniform and small compared to sonic speed and directed normally to the wire, and fluid temperature and density are constant, for equilibrium conditions $de/dt = 0$ and the Joule heating H equals the convective heat transfer Q, that is

$$I^2 R_w = \frac{\mathrm{Nu}\, k_f}{d_w} A(T_w - T_a). \tag{2.6}$$

For forced convection regime, i.e. $\mathrm{Re} > \mathrm{Gr}^{1/3}$ (0.02 in air) and $\mathrm{Re} < 140$, dimensionless heat transfer coefficient (Nu) can be written as

$$\mathrm{Nu} = A_1 + B_1 \mathrm{Re}^n = A_2 + B_2 U^n. \tag{2.7}$$

Substituting this into the above equation leads to

$$I^2 R_w = E^2 = (T_w - T_a)(A_3 + B_3 U^n) \tag{2.8}$$

which is called the King's law where it is clear that the voltage drop is a direct measure of velocity. Despite extensive work (Bruun 1995), no universal expression to describe heat transfer from hot wires exists and, thus, for the measurements, direct calibration of the anemometer and the probe was necessary.

2.3.2. System Description and Calibration

In this investigation, the anemometer was operated at constant temperature mode (CTA) in which the wire temperature was kept constant and, hence, the effect of thermal inertia is greatly reduced. This was achieved by keeping the sensor resistance constant by a servo amplifier (DANTEC 1999). The wire probe used is shown in figure 2.4. It is a cross-wire probe with wires of 5 μm diameter and 1.25 mm length,

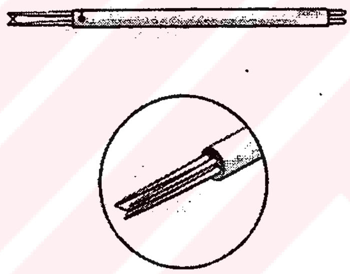

Figure 2.4 Cross-wire probe

oriented ±45 degrees to the flow. It was able to measure flow velocities within ±45 degrees with respect to the probe axis.

Velocity and direction calibrations were made at the TURNA calibration set-up, figure 2.5 that produced a low turbulence jet of 52 mm diameter. A radial blower, connected via a flexible hose to a settling chamber, pressurized air filtered through a box filter. The flow was refined from any irregularities by an arrangement with a honey comb (of passages of 5 mm effective diameter and 20 mm thickness), a wire grid of mesh size 0.25 mm^2, a second honey comb and a final wire grid in series before it was delivered through the convergent nozzle of contraction ratio of 4. The

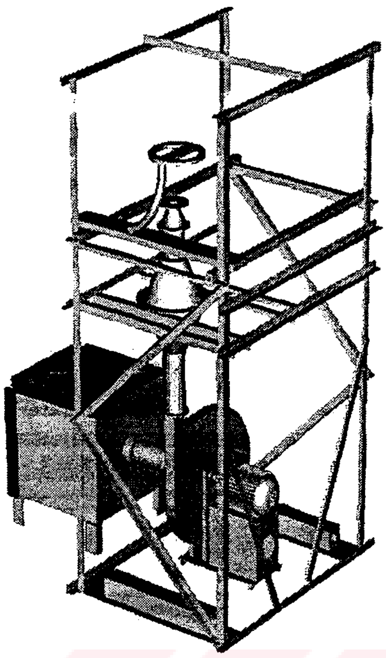

Figure 2.5 The TURNA calibration set-up

air jet at the exit had a turbulence intensity of 0.12% with boundary layer thickness of 2 mm.

Calibration was made in a range of velocities between 9 to 65 m/s at seven points against a pitot tube connected to a U-manometer of resolution of 0.5 mm water, and the velocity was determined from Bernoulli equation

$$U = \sqrt{\frac{2(P_2 - P_1)}{\rho}}. \quad (2.9)$$

The result of velocity calibration is shown in figure 2.6. It is possible to fit a curve to velocity U as function of output voltage E

$$U = C_0 + C_1 E + C_2 E^2 + C_3 E^3 + C_4 E^4 \quad (2.10)$$

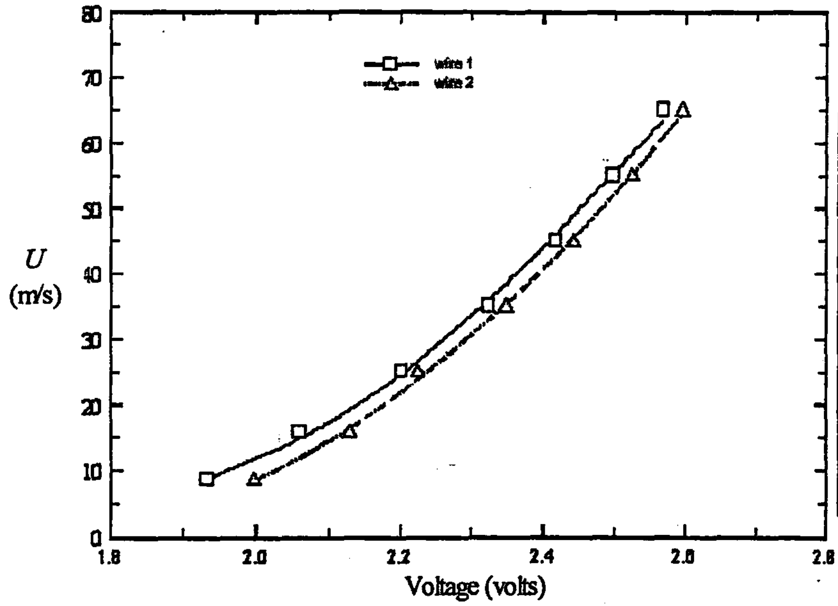

	wire 1	wire 2
C_0	-652.82	180.80
C_1	927.77	-219.74
C_2	-456.57	65.04
C_3	79.49	0.90
C_4	-.00001	0.00008

Figure 2.6 Velocity calibrations

The finite length wire (l_w/d_w~200) will have also directional sensitivity, which was exploited to measure simultaneously the two components of velocity. For the hot-wire probe used, directional sensitivity were shown in figure 2.7.

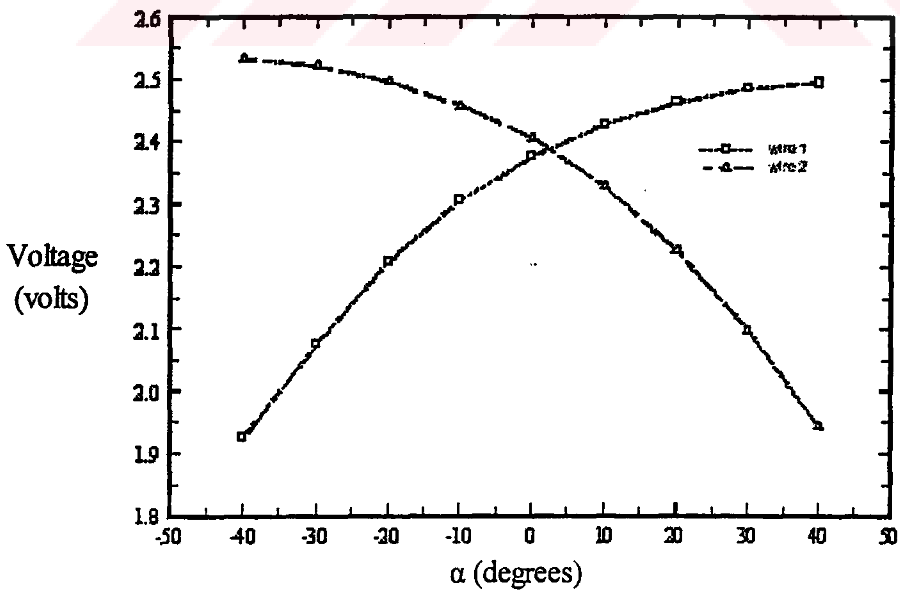

Figure 2.7 Directional calibrations

It is known that all real transducers operate with a limited temporal resolution (frequency response) which, in the present case, was the time taken by the anemometer to re-balance itself. In the present investigation, this was around 50 kHz for both wires.

2.3.3. Error Sources

Since anemometer makes use of heat transfer from the probe, anything other than the flow variable being measured that changes the heat transfer is a source of error. These include unsystematic effects such as probe vibrations and systematic effects such as ambient temperature changes and solid wall proximity. In order to avoid vibrations induced by the surroundings via the probe support, stiff and rigid probe mounts were used. Depending on the flow, vibrations of the probe prongs due to eddy shedding from them might have natural frequencies from 8 to 20 kHz, but because they have very small amplitudes, can be ignored. Heat transfer from the probe is proportional to the temperature difference between fluid and sensor and, as T_a varies, heat transfer changes as well as the fluid properties. Thus, the anemometer output depends on temperature as well as velocity and, when ambient temperature increases the velocity is measured too low, if not corrected for. To deal with temperature variations, the temperature was measured along with the anemometer voltage that was then corrected before conversion.

$$E_{corr} = \left[\frac{T_w - T_{ref}}{T_w - T_{acq}} \right]^{0.5(1+m)} E_{acq} . \qquad (2.11)$$

Selecting m = 0.2 improved compensation to better than ±0.05%/C.

2.3.4. Data Acquisition

Data acquisition, conversion and reduction were made with digital processing based on an A/D board (National Instruments AT-MIO-E-1) and signal conditioning unit (National Instruments SC 2040). The A/D board converted analogue signals into digital information (numbers) with a resolution of 16 bits. In order to avoid phase lag between sensors of the two-dimensional probe, simultaneous sampling was used. Time domain statistics require a sampling frequency twice the highest frequency of interest in the flow and, therefore, it was set to 30 kHz. 300,000 samples were acquired at each point, which was sufficient to provide stable statistics.

2.4. Data Reduction and Presentation

The origin of the frame of reference was located at the point on the ground plate where the centerline of the model intersects with the x, y and z axes representing the lateral, transversal and streamwise directions, respectively. The measurement grid extended in the lateral direction from x=-21 cm to x=11 cm and in the transversal direction from y=1 cm to y=24 cm with 1 cm interval in each direction, over 792 mesh points on a plane located 83 mm downstream the model. In order to obtain three components of the velocity field, measurements were made with cross-wire probe rotated 90 degrees at each mesh point. Two traversing systems were set, one on the top and the other on the side of the tunnel, and each consisted of a car moving on two rails oriented 10 degrees to the transversal direction. When the probe was located on the top traverse, W and U and, when it is on the side, W and V velocities were measured simultaneously. The differences of two W velocities were, in most of the region, less than 5 percent of the local value and, thus, only one of them is used. In order to reduce positioning errors, the coincidence of the side and top traverse grids was checked at least five different locations using a diode laser, which was better than 0.5 mm over the most of the grid points.

In order to avoid low frequency noise contaminating the data, each data series was high pass filtered in time domain at 70 Hz. Data was also low pass filtered at 15 kHz, half the sampling frequency. Higher order statistical moments were calculated using the general formula

$$\zeta^m = \frac{1}{N-1}\sum_N \left(\zeta - \bar{\zeta}\right)^m, \tag{2.12}$$

where ζ is a dummy variable, m is 2,3 or 4 (depending the order of moment), N is the number of data (300,000 in this case). Time-averaged-mean is defined as

$$\bar{\zeta} = \frac{1}{N-1}\sum_{N}\zeta. \tag{2.13}$$

The cross- and triple-correlations were defined as

$$\overline{\zeta^m \xi^n} = \frac{1}{N-1}\sum_{N}\left(\zeta - \bar{\zeta}\right)^m \left(\xi - \bar{\xi}\right)^n, \tag{2.14}$$

where m=1 or 2 and n=1 or 2. Data is presented with mean and rms values rendered dimensionless by the approach velocity, W_∞, and higher order moments by the corresponding rms values.

3. RESULTS AND DISCUSSION

3.1. Time-Averaged Statistics of Velocity

Experiments performed on the same model exposed to the same approach velocities but without crosswind (Kozaka *et al.* 2001) have shown that the separation from side surfaces forms a strong inward flow, which slows down towards the centerline before it merges into a vertical stream, induced by the separation from the top surface. Because of increase of the local pressure, the vertical flow accelerates below the roof until the heights close to the ground where, after deceleration, streamlines are deflected towards the sides. With the opposing inward flow from the sides, the lateral flow is then forced to turn up again, eventually forming the two distinct counter-rotating vortices. In the following, changes in this flow pattern with crosswind are discussed.

The distribution of the in-plane velocity and the corresponding contours of the $\overline{U}$ and $\overline{V}$ components the over the sampling plane were shown in figures 3.1-3 for the three configurations with $W_\infty = 18$ m/s and $U_c = 3.2$ m/s, $W_\infty = 28$ m/s and $U_c = 4.9$ m/s, and $W_\infty = 38$ m/s and $U_c = 6.7$ m/s, respectively. The vector field of figure 3.1 puts in evidence that the cross flow effectively adds a shift velocity which causes the inward flow on the right hand side to increase, while in the upper left region, the lateral velocities being either diminished or reversed. The outcome is to turn velocity vectors from right to the left. This is clearly shown on the contour plot of $\overline{U}$ where the line of zero velocity (ζ_0), separating regions of negative and positive velocities, extends roughly over the diagonal from the upper left to the bottom right, which should otherwise coincide with the line of symmetry of the model. Due to continuity, the resulting net flux of fluid increases the out-of-plane and, mostly, the vertical velocities over the upper left region immediately below the ζ_0-contour line.

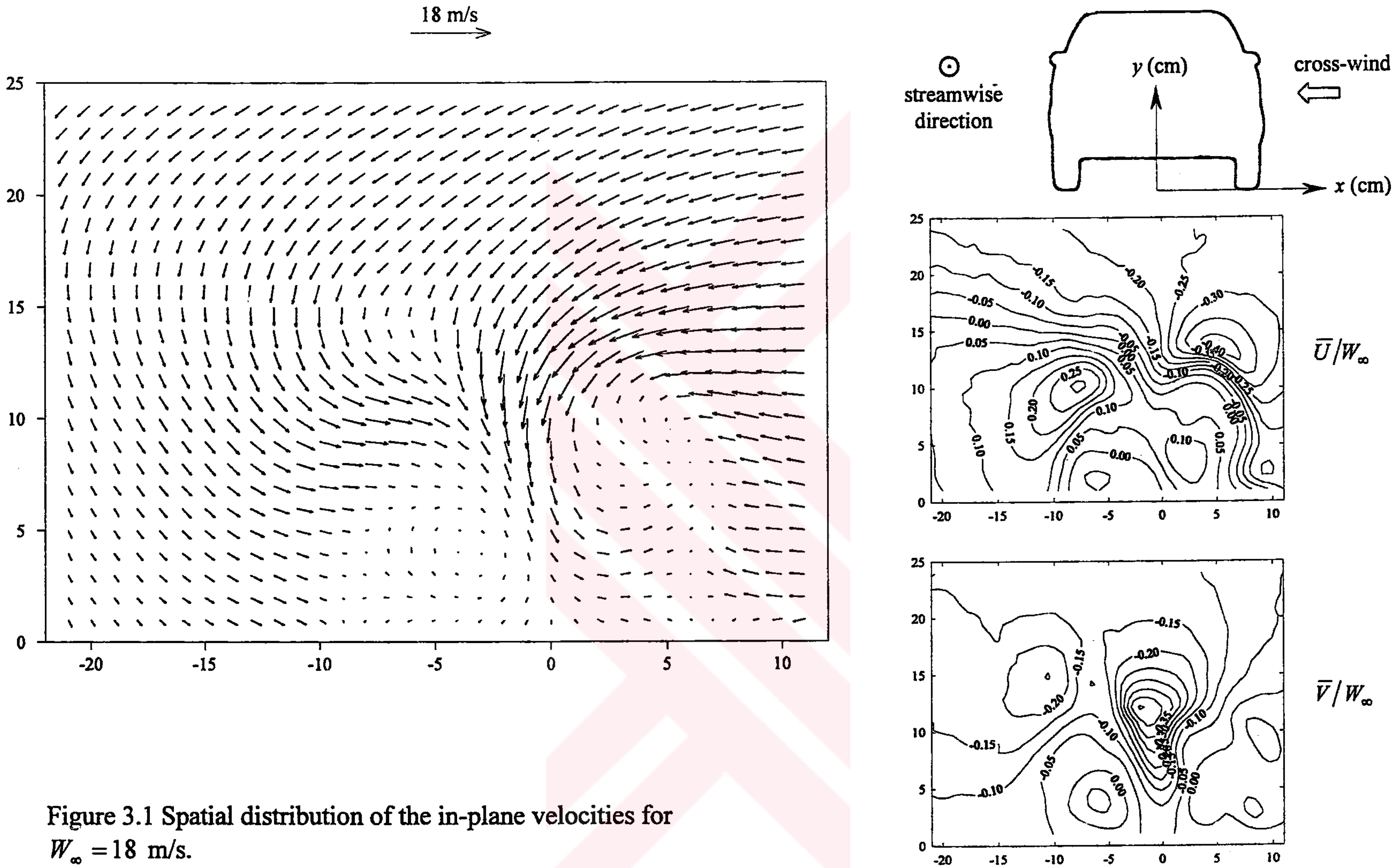

Figure 3.1 Spatial distribution of the in-plane velocities for $W_\infty = 18$ m/s.

The contours of the $\overline{V}$ velocity prove that with the exposure to the crosswind, apart from the region in vicinity of the line of symmetry, the downward velocities also appear dominantly over the area in particular under the ζ_0-contour line. However, the flux towards the left is counter balanced on this side by the increased inward velocities close to the ground. The end effect of such a flow distribution is to tilt the whole system counterclockwise, resulting in the counter-rotating vortices positioned asymmetrically on both sides of the line of symmetry. The vortex on the right hand side has been lifted up and squeezed laterally by the dynamic pressure of the cross flow, which resulted in different size measures in the x and y directions. Consequently, the location of the center of rotation of the vortex is displaced towards the upper right and stands at the end of a path through which the extremely low in-plane velocities spiral in over the boundary with the incoming crosswind. As it is shown in the following, the path of the low in-plane velocities coincides exactly with the valleys in the contours of the out-of-plane velocity, which makes a minimum at the center of rotation. The turbulence characteristics of the flow in this region are obviously expected to exhibit strong non-isotropy. The vortex on the left hand side is pushed towards the ground and, because of the spatial constraint imposed by the ground and relatively higher incoming lateral velocities, it becomes much smaller in physical size.

Figure 3.2 shows that as the approach and crosswind velocities increase, $W_\infty = 28$ m/s and $U_c = 4.9$ m/s, the domain where the shifting of lateral velocity in the direction of crosswind occurs is enlarged to cover all the upper part of the plane and, thus, the contour of zero $\overline{U}$ velocity (ζ_0) is curved further down on the left hand side. The vector plot of the in-plane velocity normalized by the approach velocity clearly shows a relative decrease of magnitudes in the lower left quadrant of the sampling plane where the flux of mass and momentum were at least partially reversed within the plane. This indicates that for this configuration large portion of the momentum added by the crosswind is transported with the out-of-plane velocities rather than being conserved within the in-plane velocities. As a result, the outward flow formed upon the deflection of the vertical stream is exposed to a much weaker resistance on the left hand side and, thus, penetrates further away from the centerline.

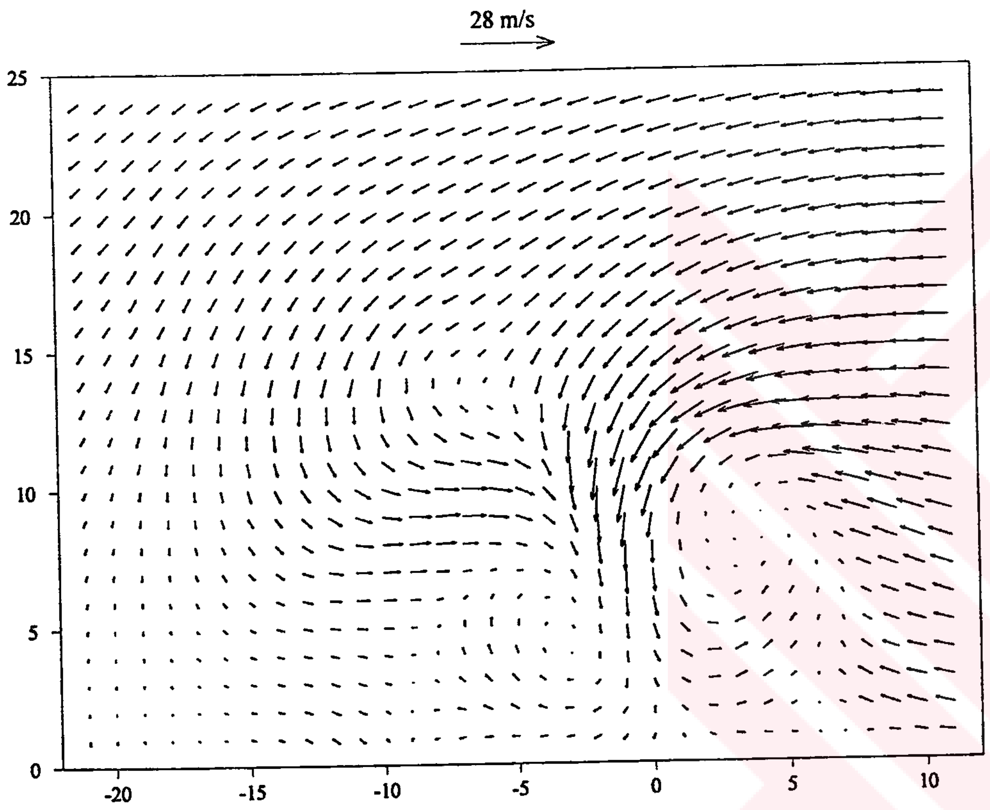

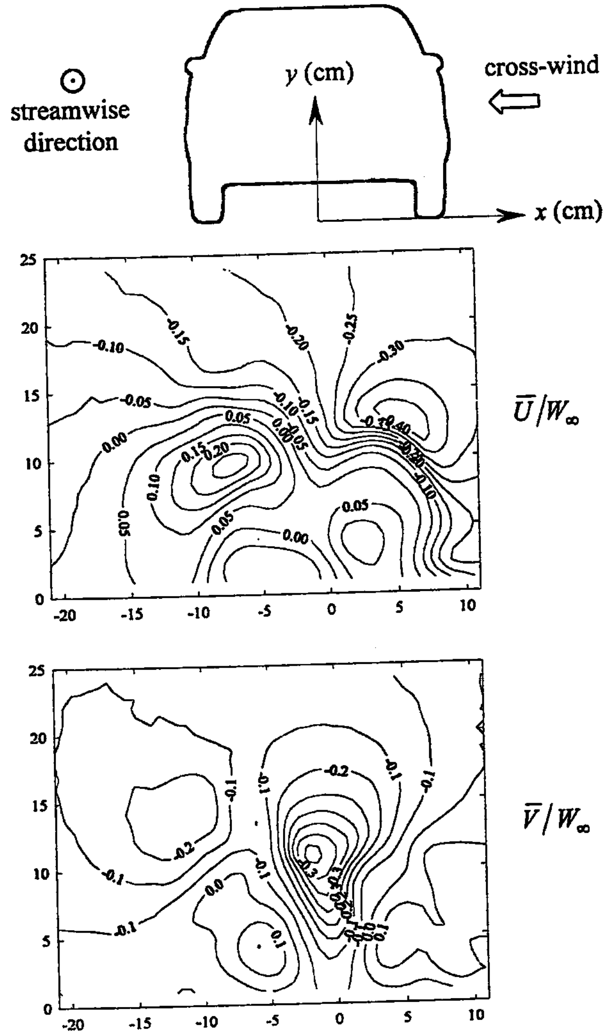

Figure 3.2 Spatial distribution of the in-plane velocities for $W_\infty = 28$ m/s.

Then, compared to the previous case, a structure of higher vorticity is formed, which allows the vortex to occupy a slightly larger space away from the ground. On the other hand, it is interesting that the relative magnitudes of the velocities involved and the size of the vortex on the right remain nearly the same as in the previous configuration. Therefore, although there is some improvement, the asymmetry of the vortices remains. As the model is exposed to even higher velocities, figure 3.3, the lateral velocity induced by the cross-flow becomes effective almost everywhere except for a small region in the wake, confined between the contour of zero $\overline{U}$ velocity (ζ_0) and the ground. The in-plane velocities in the lower left quadrant are nearly diminished in comparison to the approach velocity, which results in further strengthening of the vortex on the left. The vortex on the right again seems to be qualitatively unaffected from the changes in the approach and crosswind velocities.

The streamwise vorticity, figure 3.4, shows that two positive peaks asymmetrically located on both sides of the centerline dominate the distribution. The one on the right has definitely higher values and larger spatial structure, which remains unchanged with increasing approach and crosswind velocities. Because of this and from the space it occupies, it can be deduced that it is associated with the flow field around the vortex on the right. The positive peak on the left is located well clear of the ground and stems from the flow rapidly turning to the right to compensate the lateral mass flux due to added velocity of the cross-wind. It can hardly be noticed that in between these two positive peaks, there occurs a negative peak due to the vortex on the left. It is very revealing that with increasing approach velocity while the positive peak on the left weakens, the negative peak due to the vortex on the left gains further strength.

The distributions of the out-of-plane velocity, shown in figure 3.5, map the region of velocity defect for the three approach velocities. The shear layers surrounding the core region are characterized by sharp velocity gradients, which are easy to identify with closely spaced lines. On both sides of the core region, these lines tend to close and form two lobes with contours curling up from the ground, which indicate zones of extremely low velocities. It is interesting that spatial distribution of these contours exactly coincide with the locations where the low in-plane velocities are seen.

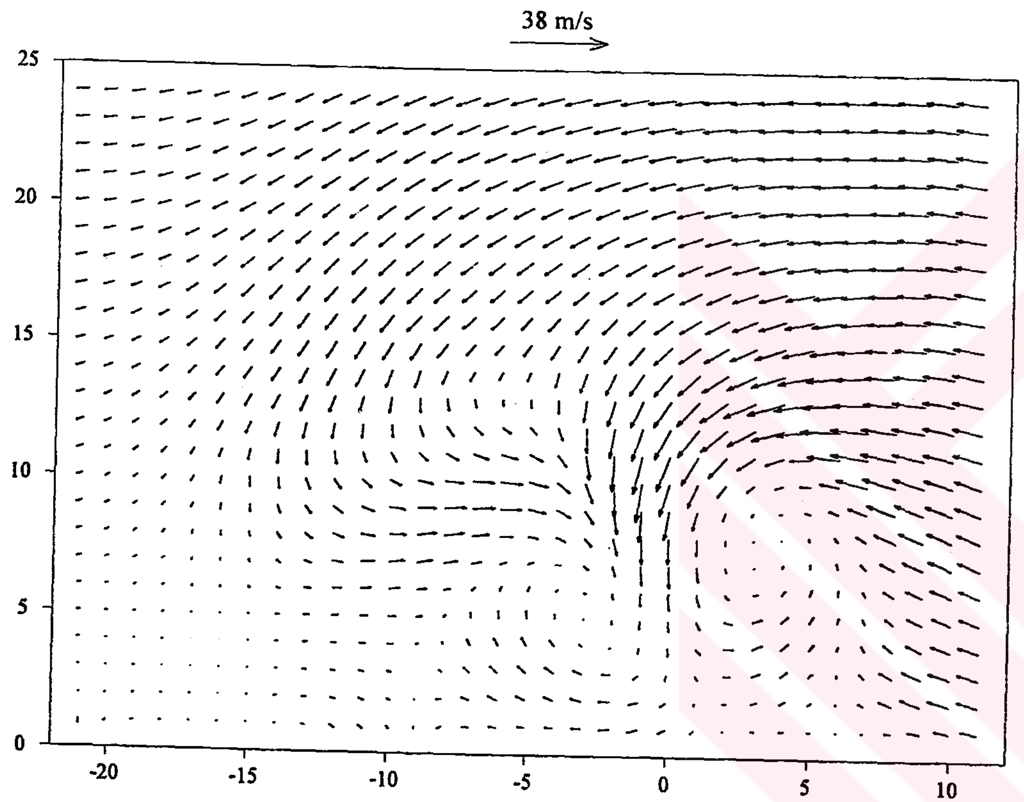

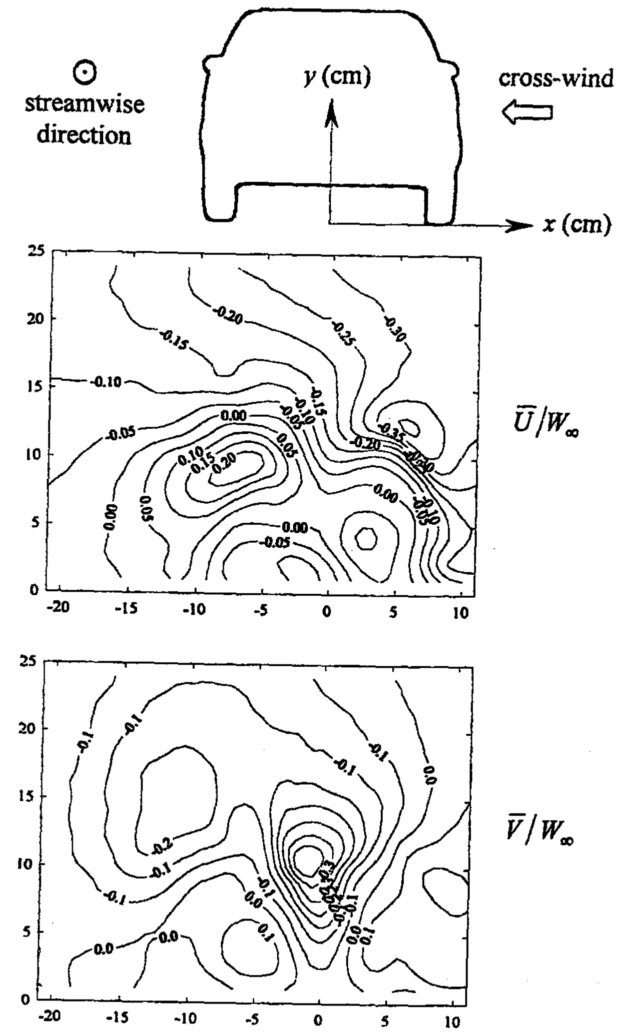

Figure 3.3 Spatial distribution of the in-plane velocities for $W_\infty = 38$ m/s.

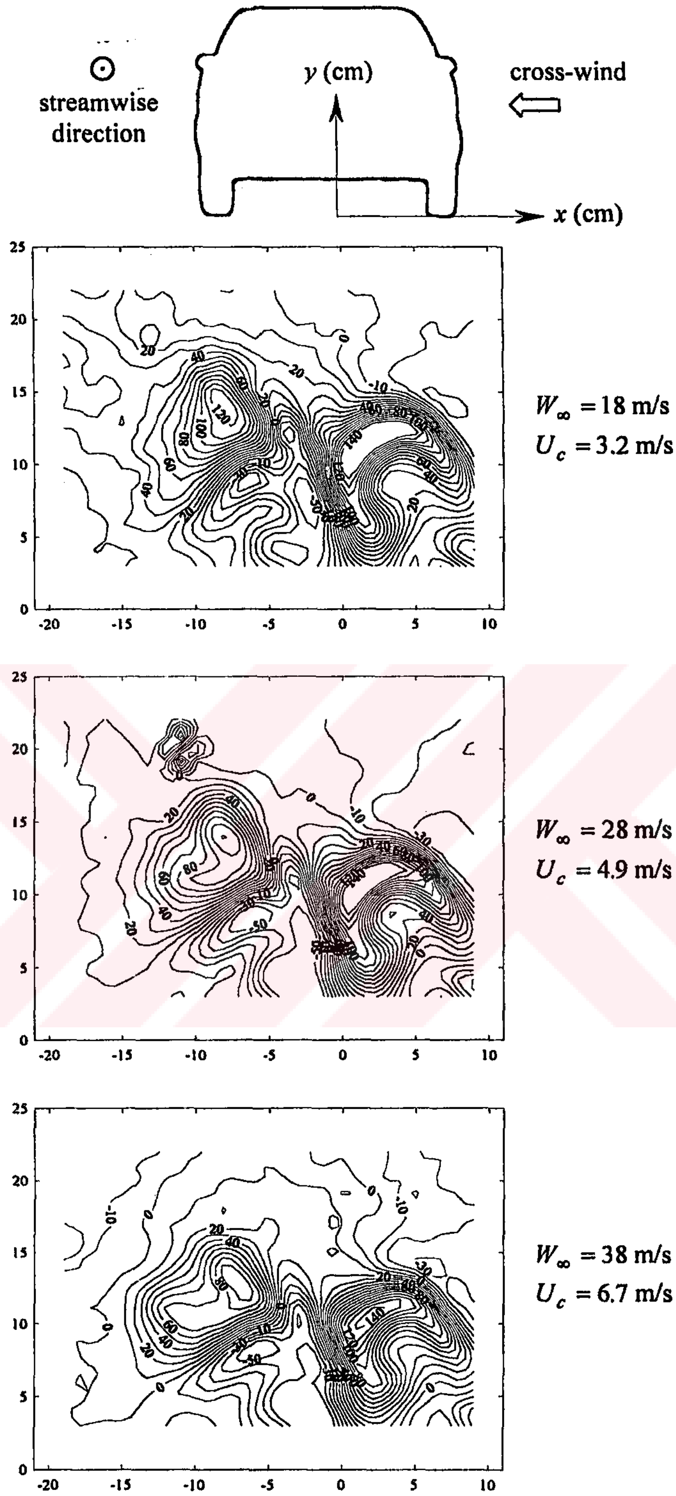

Figure 3.4 Spatial distribution of the streamwise vorticity, $\Omega_z / W_\infty L_F$.

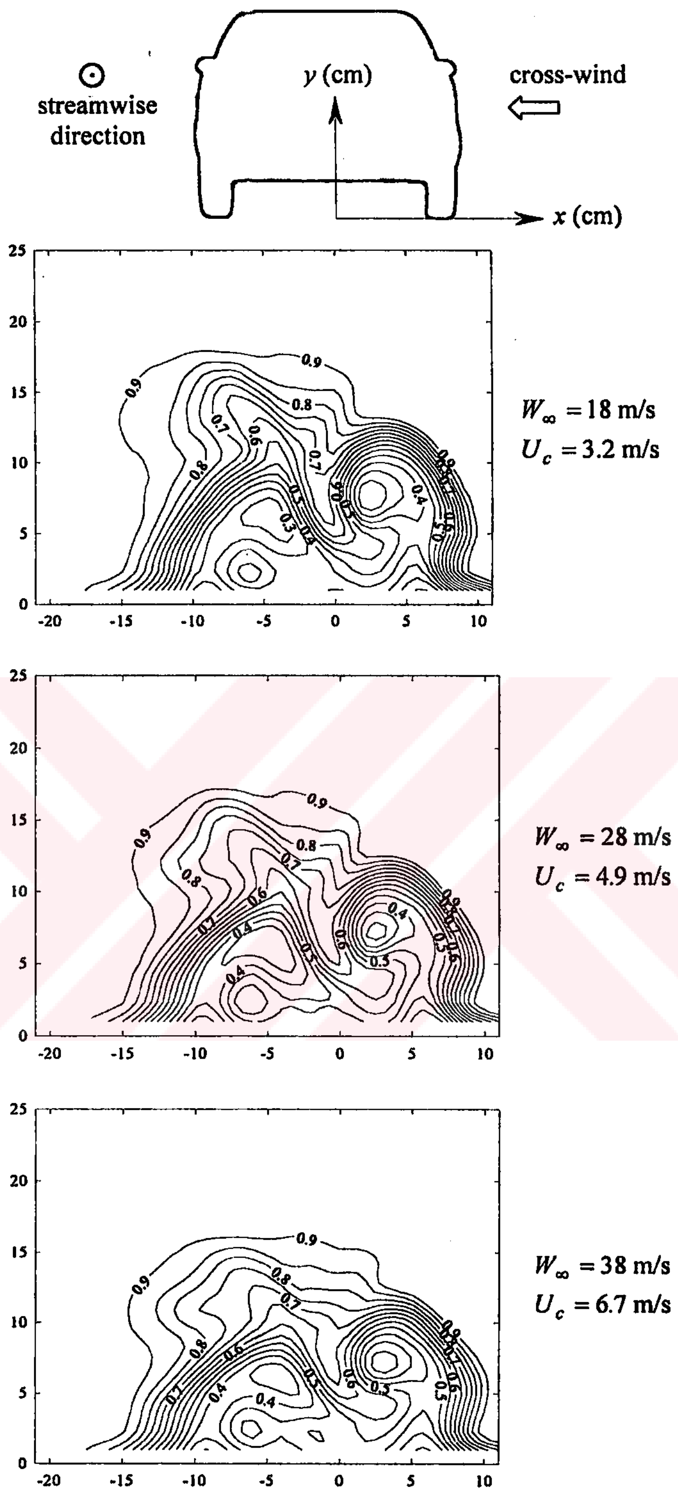

Figure 3.5 Spatial distribution of the streamwise mean velocity, $\overline{W}/W_\infty$.

Therefore, it can be concluded that the flow field of the counter-rotating vortices revealed by the in-plane velocity distribution is indeed a two dimensional vector map of two counter-rotating helical structures. Nevertheless, as the cross-section of the structure grows further downstream, it is expected that the rate of rotation will diminish and the streamwise velocity will become uniform inside the helix. It should also be noted that the in-plane velocities induced by the crosswind convect a significant amount of streamwise momentum defect both in the x and y-directions. As a result, relatively milder velocity gradients appear, in particular, at the upper left part of the wake region. As the approach velocity increases the topology of the streamwise velocity remains qualitatively the same, although there occur some suppression in the vertical direction. It should be mentioned that near the ground, contour lines tail outwards, which is a consequence of the boundary layer developing over the non-moving ground. However, this effect seems to be confined within a distance less than 2 cm above the ground, which corresponds to less than 10% of the total height of the model.

The spatial distributions of the rms velocities are presented in figures 3.6-8. The shear layer surrounding the wake region comes out in all the figures, indicating that in this region turbulent kinetic energy has contributions equally well from all directions. Apart from this region, which is expected to have an isotropic turbulence, different zones are dominated by fluctuation energy of different turbulent components. Figure 3.6 clearly shows that the flow separated from the side surfaces (figure 3.5) forms two distinct lobes, which seem to be the main source of instability driving the turbulence in the x-direction. The lobes of high turbulence seen in this figure are, however, disconnected on the top where the vertical flow heading down near the centerline (see also figure 3.7) has a significant contribution to the turbulence in the y-direction. It is very surprising that the in-plane turbulence observed in regions occupied by the counter-rotating vortices (seen in figures 3.6 and 3.7) remains relatively small compared to high values of $\sqrt{\overline{w^2}}/W_\infty$ in figure 3.8. This reveals that the axes of the counter-rotating helical structures are wandering around a mean path. It should be noted that the effect of the crosswind is particularly apparent on the left lobe, which expands both in the x and y directions. As the approach velocity increases, because the out-of-plane convection becomes dominant means of

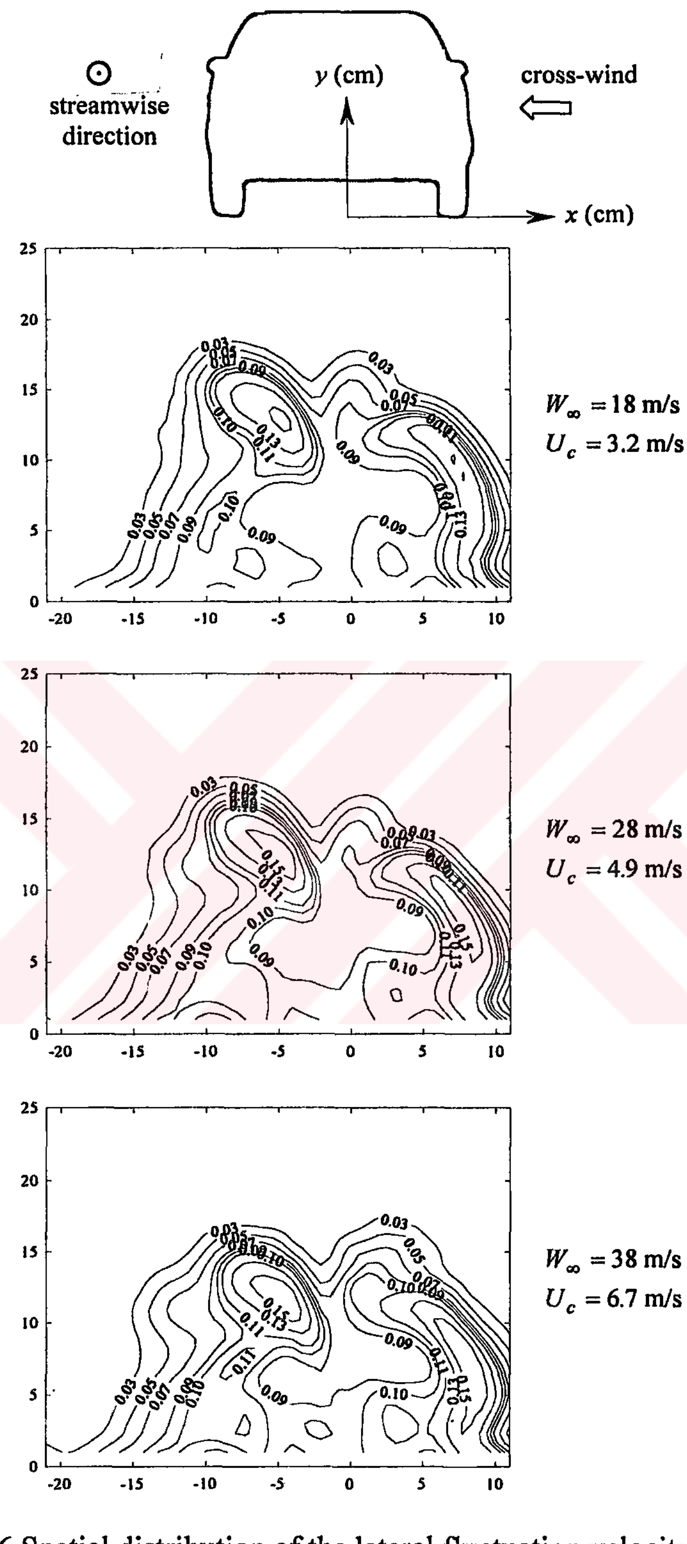

Figure 3.6 Spatial distribution of the lateral fluctuation velocity, $\sqrt{\overline{u^2}}/W_\infty$.

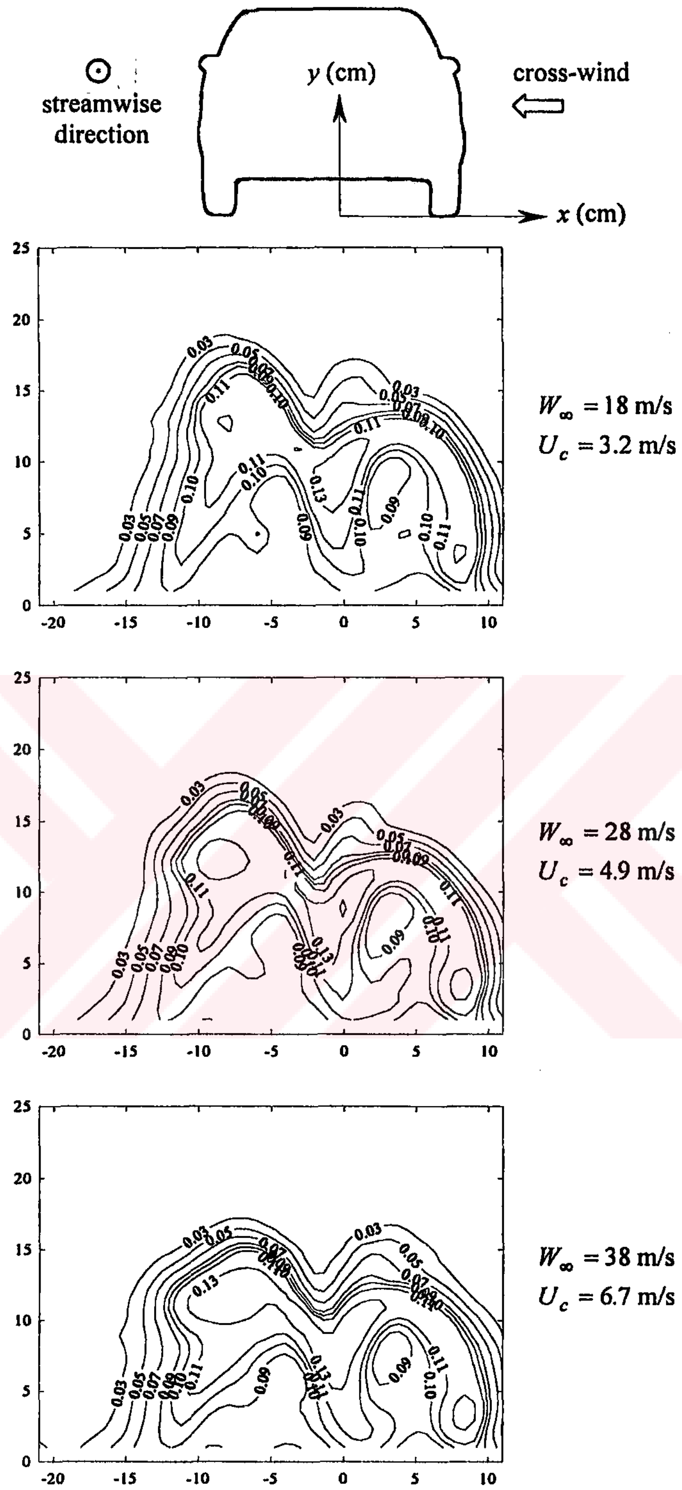

Figure 3.7 Spatial distribution of the transversal fluctuation velocity, $\sqrt{\overline{v^2}}/W_\infty$.

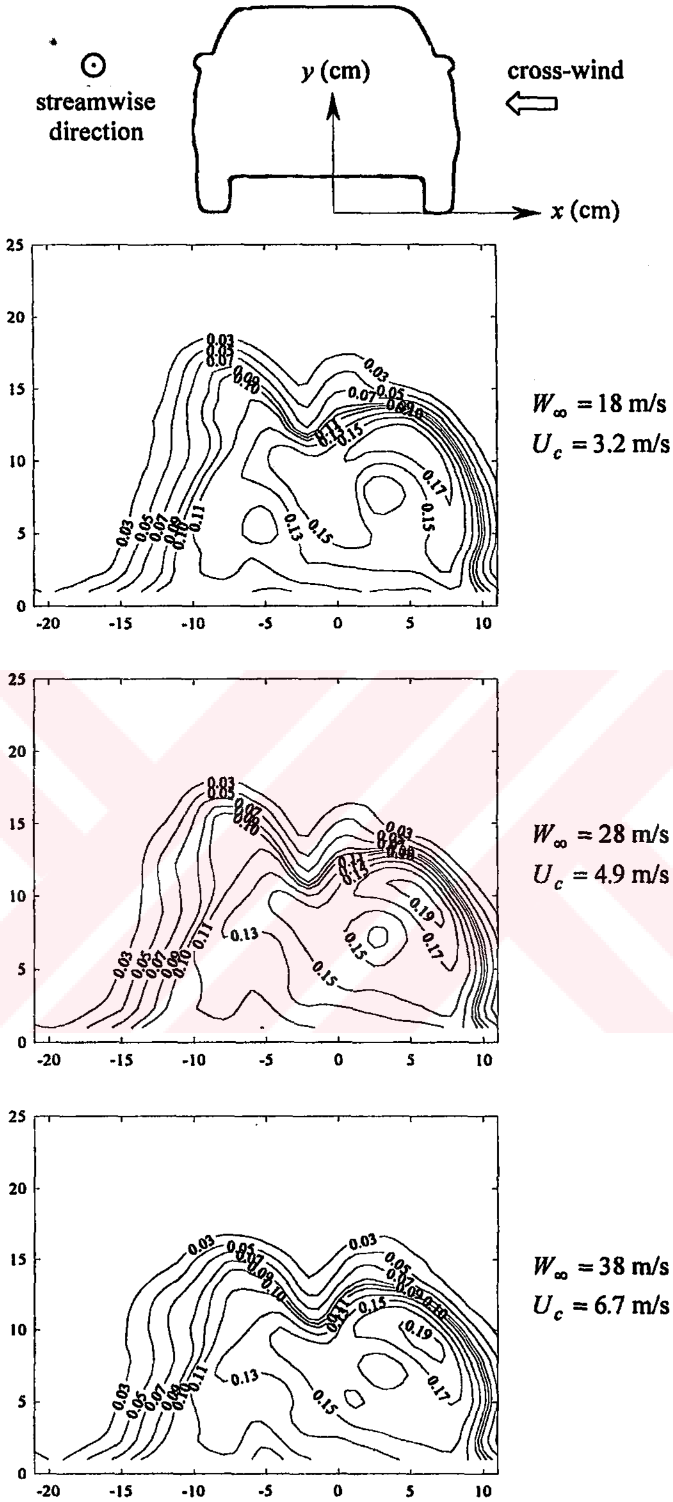

Figure 3.8 Spatial distribution of the streamwise fluctuation velocity, $\sqrt{\overline{w^2}}/W_\infty$.

turbulent transport, the acquisition of turbulence by relatively non-turbulent flow above the wake region is suppressed. In an attempt to investigate budget of turbulent kinetic energy and determine interactions and energy transfer between different components (Townsend 1976), the distribution of turbulent stresses and the production of the in-plane turbulent kinetic energy are discussed in the following. Two of the off-diagonal turbulent stresses, which play a dominant role in momentum transfer by turbulent motion, are shown in figure 3.9. The plots on the left column show that in the regions where the flow is predominantly in the *z*-direction and where a strong vertical flow occurs, the normalized shear stress, $-\overline{wu}\Big/\left(\sqrt{\overline{w^2}}\sqrt{\overline{u^2}}\right)$, attains positive values. On the other hand, in the regions where the in-plane velocity vector sharply changes its direction, like flows streaming into the counter-rotating vortices, there occur negative islands. Of these, while the one located above the vortex on the right is very large and persistent, the other seems to diminish with the increasing approach velocity. Similar topological features are also prevalent on shear stress distributions shown on the column on the right where positive peaks are more distinctive as for example the one on the upper left of the core region. The Reynolds stresses determine the exchange of energy between the mean flow and the turbulence by deformation work or turbulence production terms (Tennekes and Lumley 1972) like

$$-\overline{wu}\left[\frac{1}{2}\left(\frac{\partial \overline{W}}{\partial x}+\frac{\partial \overline{U}}{\partial z}\right)\right] \tag{3.1}$$

or

$$-\overline{wv}\left[\frac{1}{2}\left(\frac{\partial \overline{W}}{\partial y}+\frac{\partial \overline{V}}{\partial z}\right)\right]. \tag{3.2}$$

Since the streamwise gradient of the components of the mean velocity, $\partial/\partial z$, cannot be obtained from the measurements made for this investigation, the turbulence production associated with the in-plane gradients are calculated and results are presented in figure 3.10. Based on distributions on the left, it can be concluded that except for the shear layers where the wake region is directly exposed to the crosswind and where the vertical stream heading down near the centerline, there

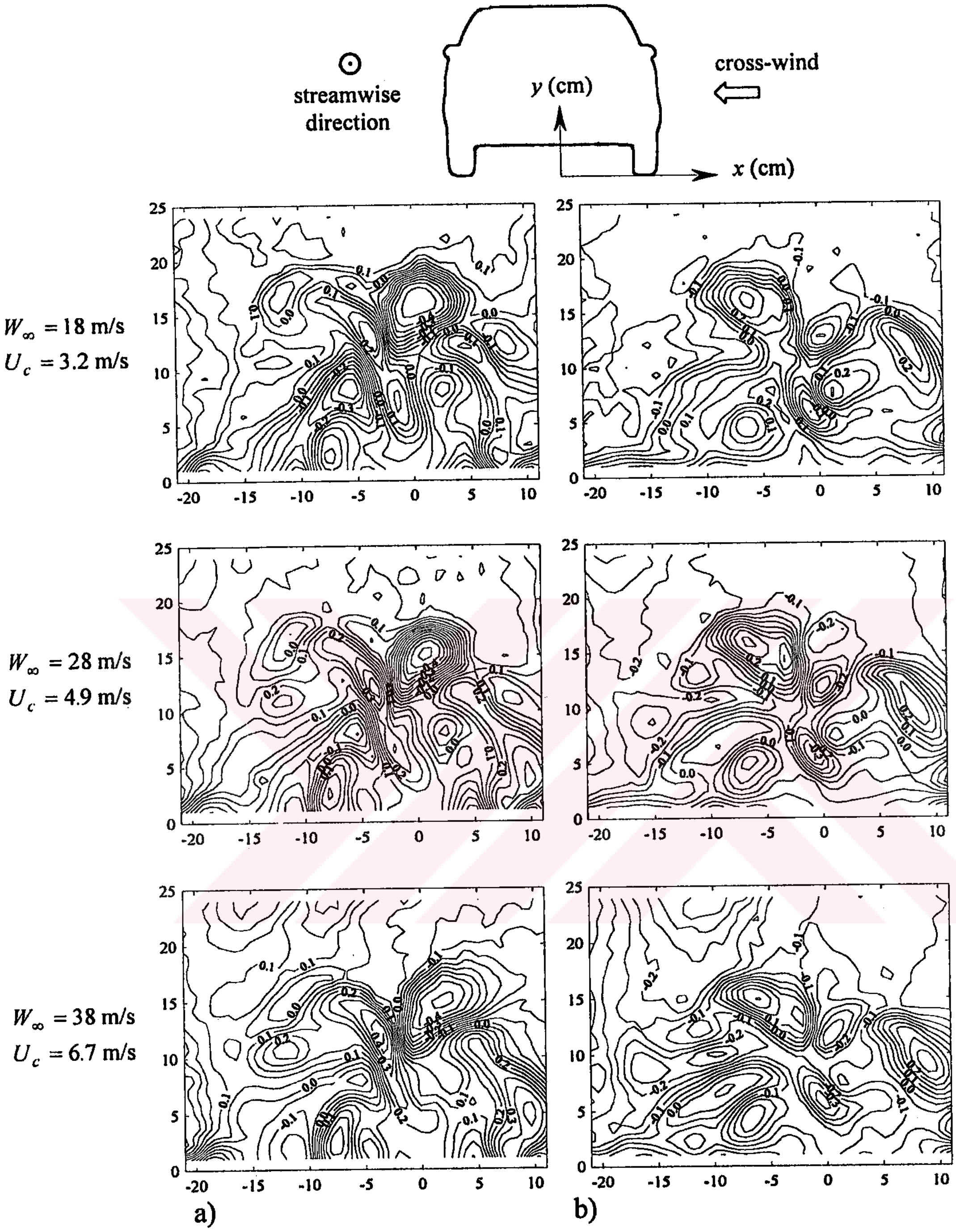

Figure 3.9 Spatial distribution of the turbulent stresses;

$$\text{a) } -\overline{wu}\Big/\left(\sqrt{\overline{w^2}}\sqrt{\overline{u^2}}\right), \text{ b) } -\overline{wv}\Big/\left(\sqrt{\overline{w^2}}\sqrt{\overline{v^2}}\right).$$

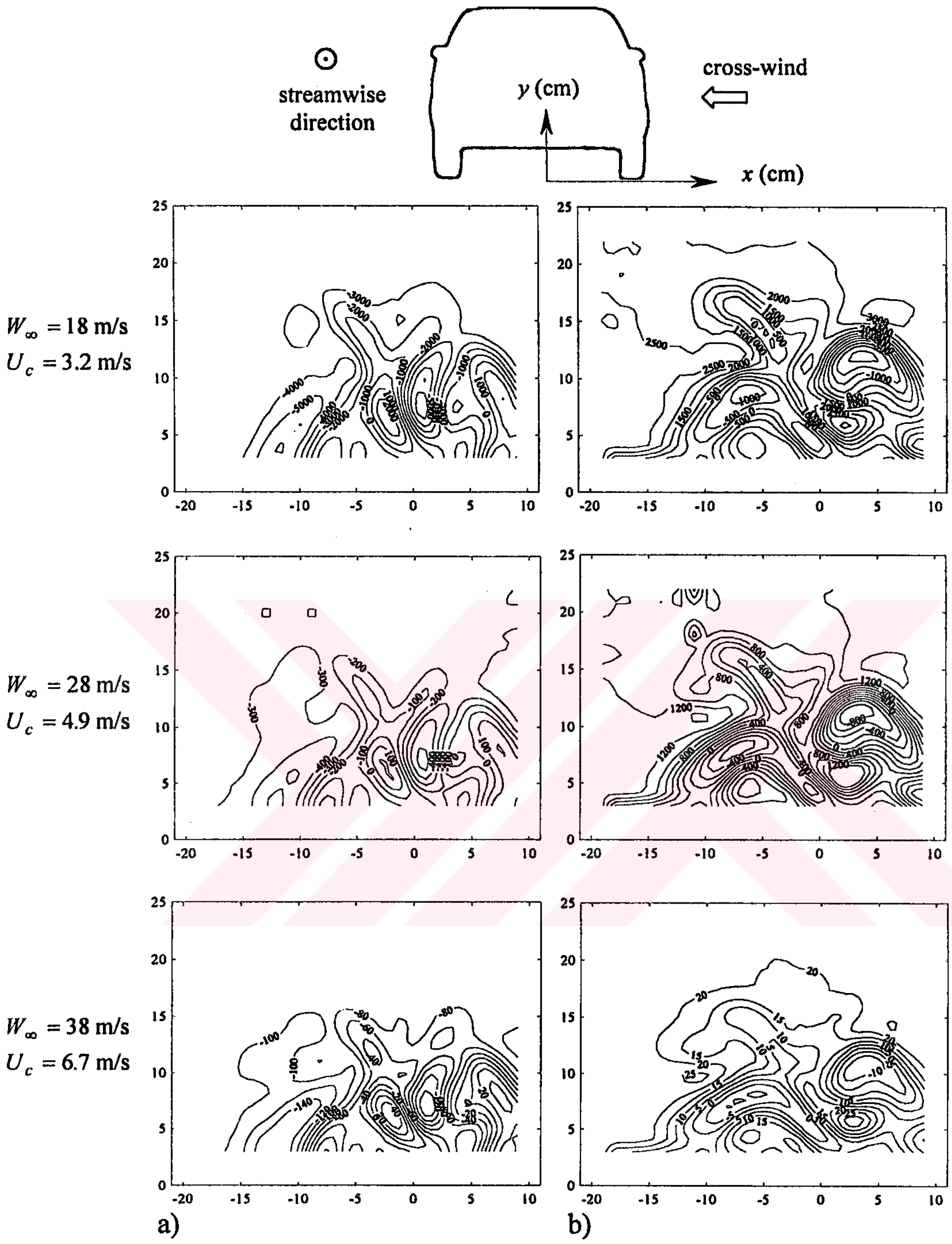

Figure 3.10 Production of turbulent kinetic energy;

$$\text{a) } -wu\left(\frac{1}{2}\frac{\partial \overline{W}}{\partial x}\right)\left(\frac{L_F}{W_\infty^3}\right)\times 10^{10},\ \text{b) } -wv\left(\frac{1}{2}\frac{\partial \overline{W}}{\partial y}\right)\left(\frac{L_F}{W_\infty^3}\right)\times 10^{10}.$$

occurs a reverse cascade (variously called back-scatter), that is, the energy is transferred from the turbulence to the mean flow. However, the energy exchange rapidly diminishes with increasing approach velocity and becomes only 2.5% of the initial amount when the approach velocity is doubled. On the other hand, distributions on the right show that, except for the flows streaming into the counter-rotating vortices, the production is positive everywhere. This means that the vortex system puts the energy back into the mean flow. This makes sense considering the fact that the vortex centers are indeed the manifolds leaking the turbulent energy out of the plane motion. It is the energy, which was already extracted from the mean flow via processes leading to the vortex formation in the core of the wake. Here again, the energy in transit decreases with the approach velocity.

The gradient of triple-correlations represents the transport of turbulent kinetic energy by turbulent fluctuations. Two peaks of opposite signs at the upper part of the core region, which are slightly skewed downwards near the centerline, dominate distributions of the triple-correlation associated with lateral transport, shown in figure 3.11*a*. These peaks are followed by two side lobes of opposite sign, which extend towards the ground and enclose the core region where the correlation becomes zero. The magnitudes involved in the structures at sides are comparatively small. Contour plots of the triple-correlation associated with transversal diffusion, figure 3.11*a*, shows negative values over the shear layer surrounding the core, and zero otherwise. The maps of energy flow corresponding to the triple-correlations discussed are given in figure 3.12. The lateral transport (column a) exhibits strong convection towards center at the upper part of the core region; exactly the same location where two peaks of opposite sign appears on the correlation distribution. On the right hand side, the inward convection has root as far as into the side shear layer whereas on the left, starting from the edge of the model (roughly x=-3 cm), the flow of energy turns outwards. Figure 3.12*a* also shows another peak on the right, located slightly inside the shear layer and above the ground, which also indicates an outward flow of energy. The map of transversal diffusion of kinetic energy, figure 3.12*b*, shows two layers of opposite sign, spread over the upper part of the core region. The layer on the top coincides with the shear layer and has positive values, indicating a flow of kinetic energy mainly in upward direction. This is attributed to the

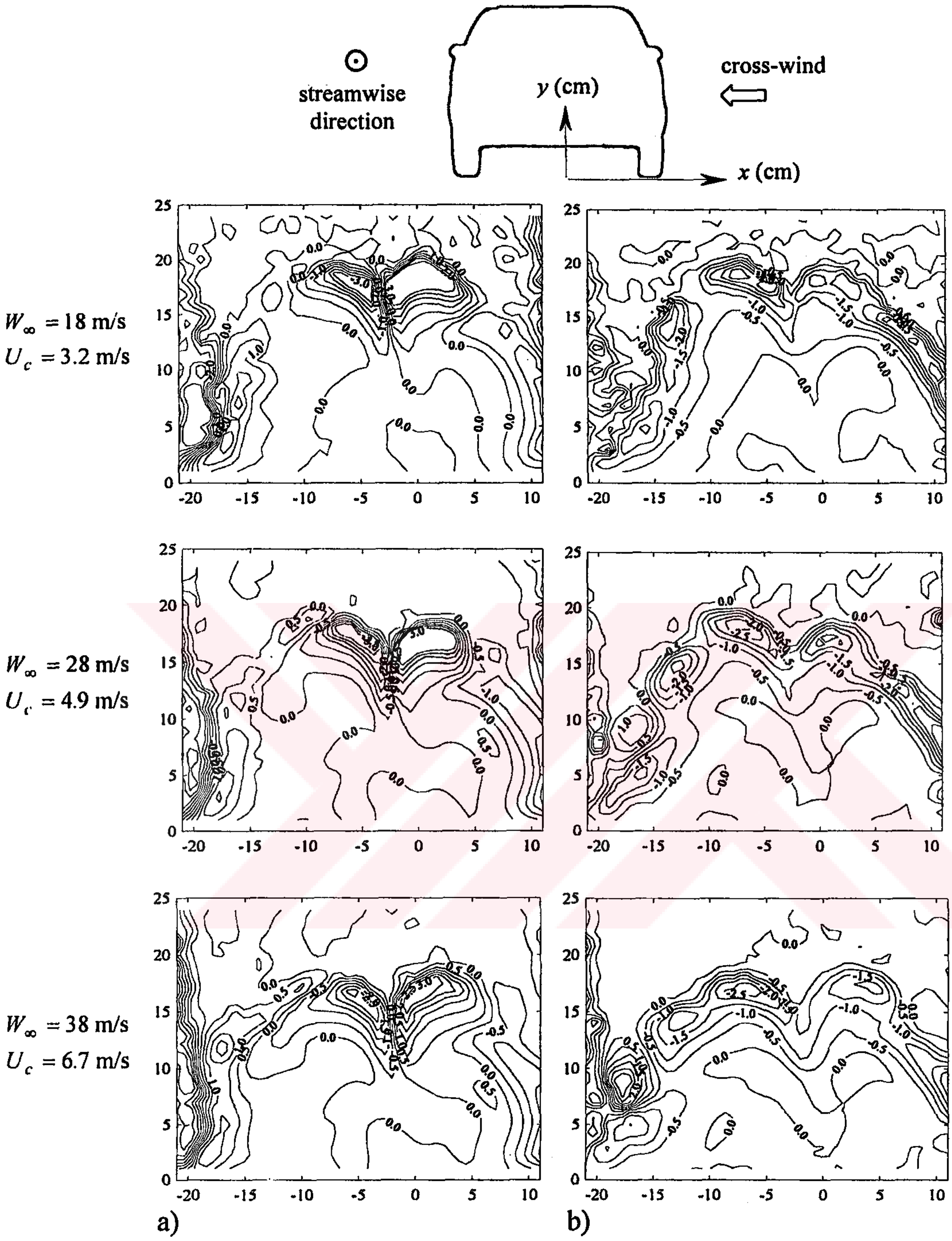

Figure 3.11 Triple-correlations between in-plane velocities and in-plane components of turbulent kinetic energy;

$$\text{a)}\ -\overline{uu^2}\Big/\left(\sqrt{\overline{u^2}}\right)^3 \quad \text{b)}\ -\overline{vv^2}\Big/\left(\sqrt{\overline{v^2}}\right)^3.$$

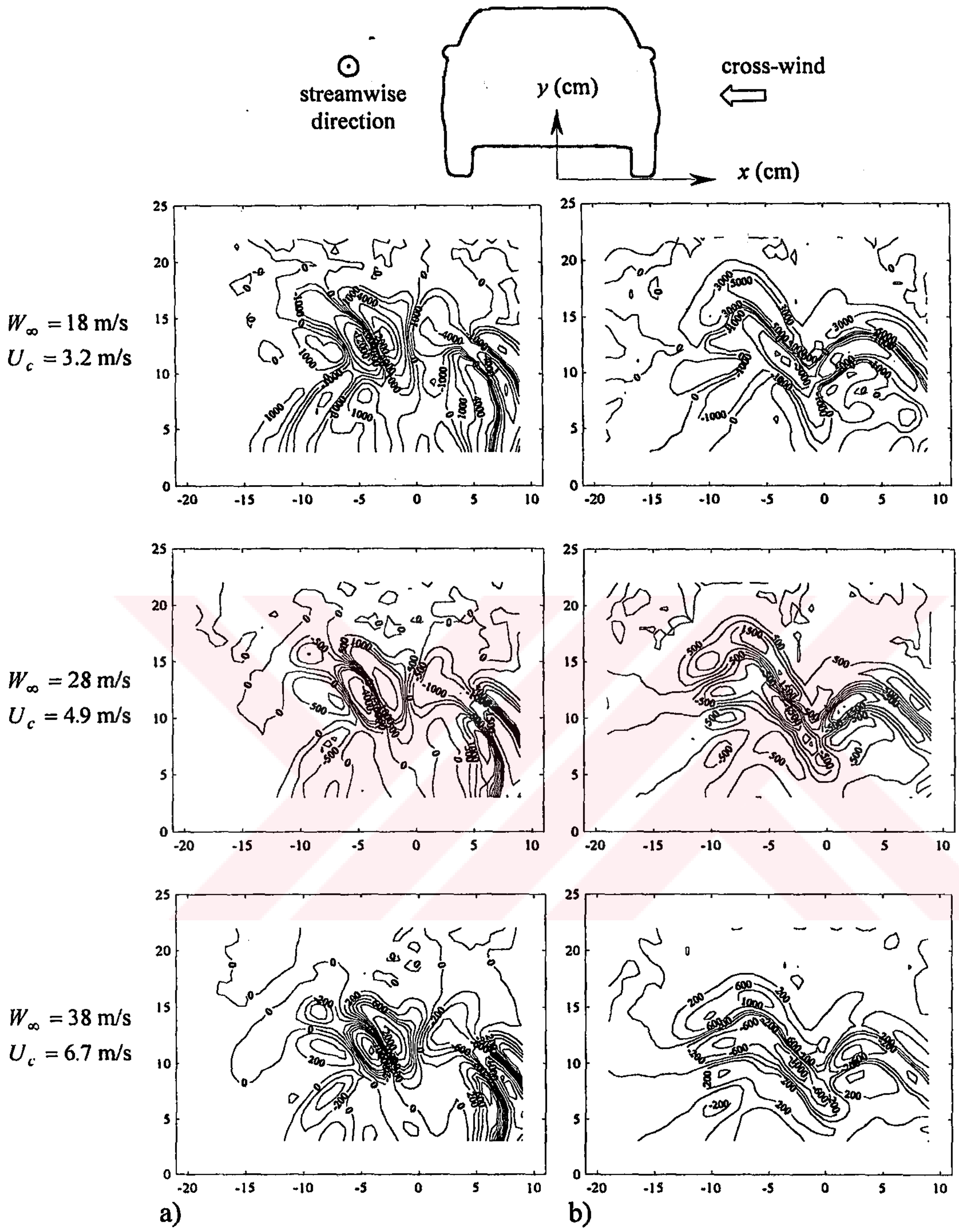

Figure 3.12 In-plane transport of in-plane components of turbulent kinetic energy;

$$\text{a)}\ -\frac{\partial}{\partial x}\left(\frac{1}{2}\overline{uu^2}\right)\left(\frac{L_F}{W_\infty^3}\right)\times 10^{10},\ \text{b)}\ -\frac{\partial}{\partial y}\left(\frac{1}{2}\overline{vv^2}\right)\left(\frac{L_F}{W_\infty^3}\right)\times 10^{10}.$$

acquisition of turbulence by the flow outside the wake region. The lower layer deforms deep into the core region and has negative values, indicating a downward flow of energy. In order to have complete picture of turbulent diffusion from one point in the plane of measurement to another, knowledge of streamwise transport would be necessary. This is because the related terms in turbulence kinetic energy equation are divergences of the energy flux (Özdemir 2001). However, since the measurements in the present investigation were made over single plane, it was not possible to obtain the streamwise gradients. Therefore, in the following, whenever information of turbulent diffusion in the z-direction is necessary, discussion will be carried, rather conjectural, on the triple-correlations involved. The triple-correlations associated with the streamwise transport of the in-plane components of turbulent kinetic energy are shown in figure 3.13. The lateral component multiplied by streamwise fluctuation velocity (column a) exhibits positive values in the shear layer surrounding the core of the wake region and in the region where the vertical stream is heading down in the vicinity of the centerline. The highest values are observed at the upper part of this region where, considering the shear layer is enclosing the wake domain, large values of streamwise derivatives are also likely to occur, which would lead to an energy exchange with the neighbouring zones. The region occupied by the two counter-rotating vortices, however, possesses larger negative values and, if the same reasoning holds valid, it also acts like a manifold where turbulent energy flows into or out of the plane. Considering the fact that in these regions, there appeared a reverse cascade, the direction of energy flow is most likely to out of plane that is in the downstream direction. Based on the unchanged topology, it is also worth noting that the energy flux out of and into the plane is relatively insensitive to the approach velocity. Distributions of the other triple-correlation, shown in column b, imply that there is a high possibility of the energy exchange, taking place in the shear layer on both sides. In between the shear layers and particularly in the core region, the energy transport may be relatively weak. The triple-correlations associated with the streamwise component of turbulent kinetic energy are shown in figure 3.14. Distributions of streamwise kinetic energy multiplied by lateral velocity are very similar to those of the figure 3.11*a*. This puts in evidence that the features determining the characteristics of these two distributions are not those of kinetic energies, $\overline{u^2}$ or $\overline{w^2}$ but of the fluctuation velocity u. Indeed, close examination of

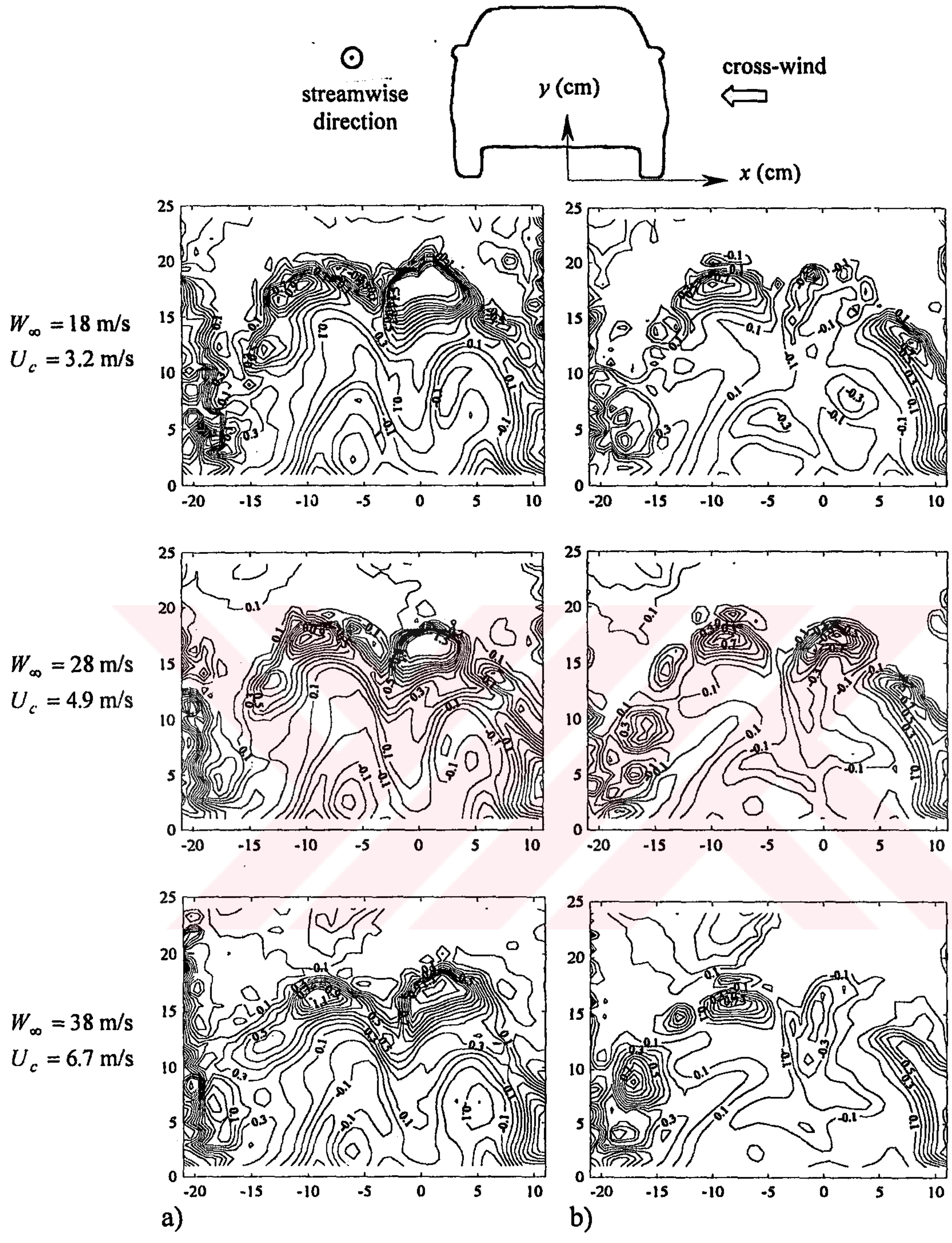

Figure 3.13 Triple-correlations between streamwise velocity and in-plane components of turbulent kinetic energy;

$$\text{a) } -\overline{wu^2}\Big/\left(\sqrt{\overline{w^2}}\sqrt{\overline{u^2}}\sqrt{\overline{u^2}}\right),\ \text{b) } -\overline{wv^2}\Big/\left(\sqrt{\overline{w^2}}\sqrt{\overline{v^2}}\sqrt{\overline{v^2}}\right).$$

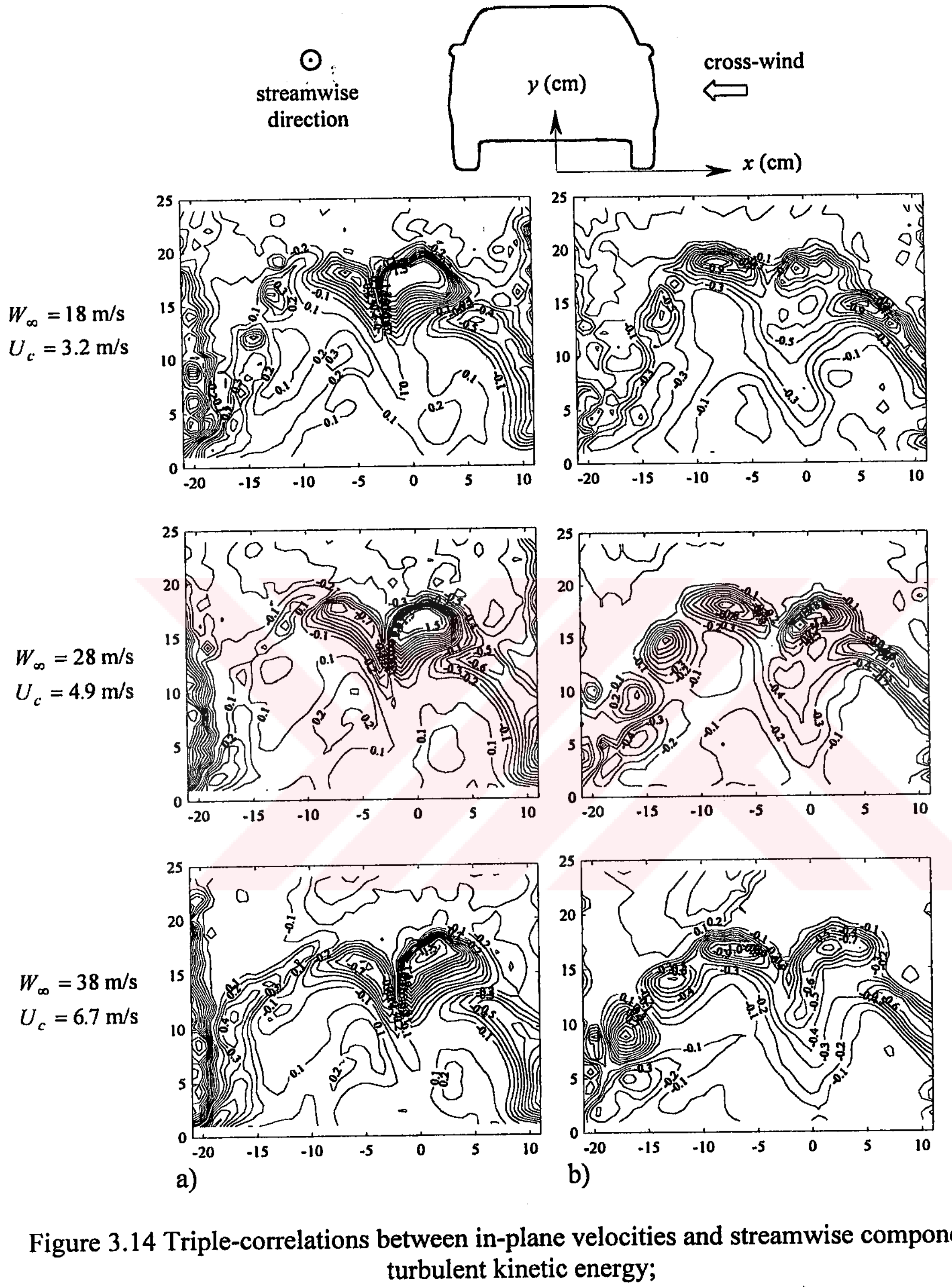

Figure 3.14 Triple-correlations between in-plane velocities and streamwise component of turbulent kinetic energy;

$$\text{a) } -\overline{uw^2}\Big/\left(\sqrt{\overline{w^2}}\sqrt{\overline{w^2}}\sqrt{\overline{u^2}}\right),\ \text{b) } -\overline{vw^2}\Big/\left(\sqrt{\overline{w^2}}\sqrt{\overline{w^2}}\sqrt{\overline{v^2}}\right).$$

figure 3.6 proves this assertion. Similar argument seems equally valid for the distributions of the triple-correlation $\overline{vw^2}$, which exhibits close resemblance to figure 3.11*b*, and both are dominated by the features of *v* presented in figure 3.7. The corresponding maps of energy transport are shown in figure 3.15 and, as it is expected look very much like the distributions shown in figure 3.12. The differences are limited to minor deformations introduced by distributions due to different components of the kinetic energy. The triple-correlation associated with streamwise turbulent kinetic energy multiplied by streamwise fluctuation velocity is presented in figures 3.16. It is clear that almost no structure can be recognized except for the shear layer surrounding the core of the wake region and this pattern seems very similar to that of the fluctuation velocity seen in figure 3.8. Finally, it is common in all the distributions associated with the triple-correlations that the magnitudes seem to decrease in much higher rate than the rate of increase of the approach velocity, which is in agreement with the decrease of the rate of production of the turbulent kinetic energy.

The statistical nature of turbulence is also of interest and figures 3.17-19 show the fourth order moments (or variously called, flatness or kurtosis) of velocity fluctuations. It is common in all the plots that except for the shear layer around the core of the wake, flatness attains values very near to 3, indicating that statistics of the fluctuations follow Gaussian distribution. In the shear layer, velocity statistics exhibit leptokurtic distributions. Gaussian type statistics is also confirmed by values of the third order moments (skewness) near zero.

3.2. Estimation of the Forces Applied by Momentum Flux

The descriptions of the mean velocity given in the previous section can be further exploited to calculate the difference of the *x*-, *y*- and *z*-momentum between the two planes before and after the model (see figure 3.20). Although it is not exact, momentum can give an estimate of the forces applied on the body at different approach and crosswind conditions. Assuming a uniform approach velocity and crosswind speed at the plane upstream, the deficit of momentum flux in the *x*-, *y*- and *z*-directions at the plane downstream can be written as

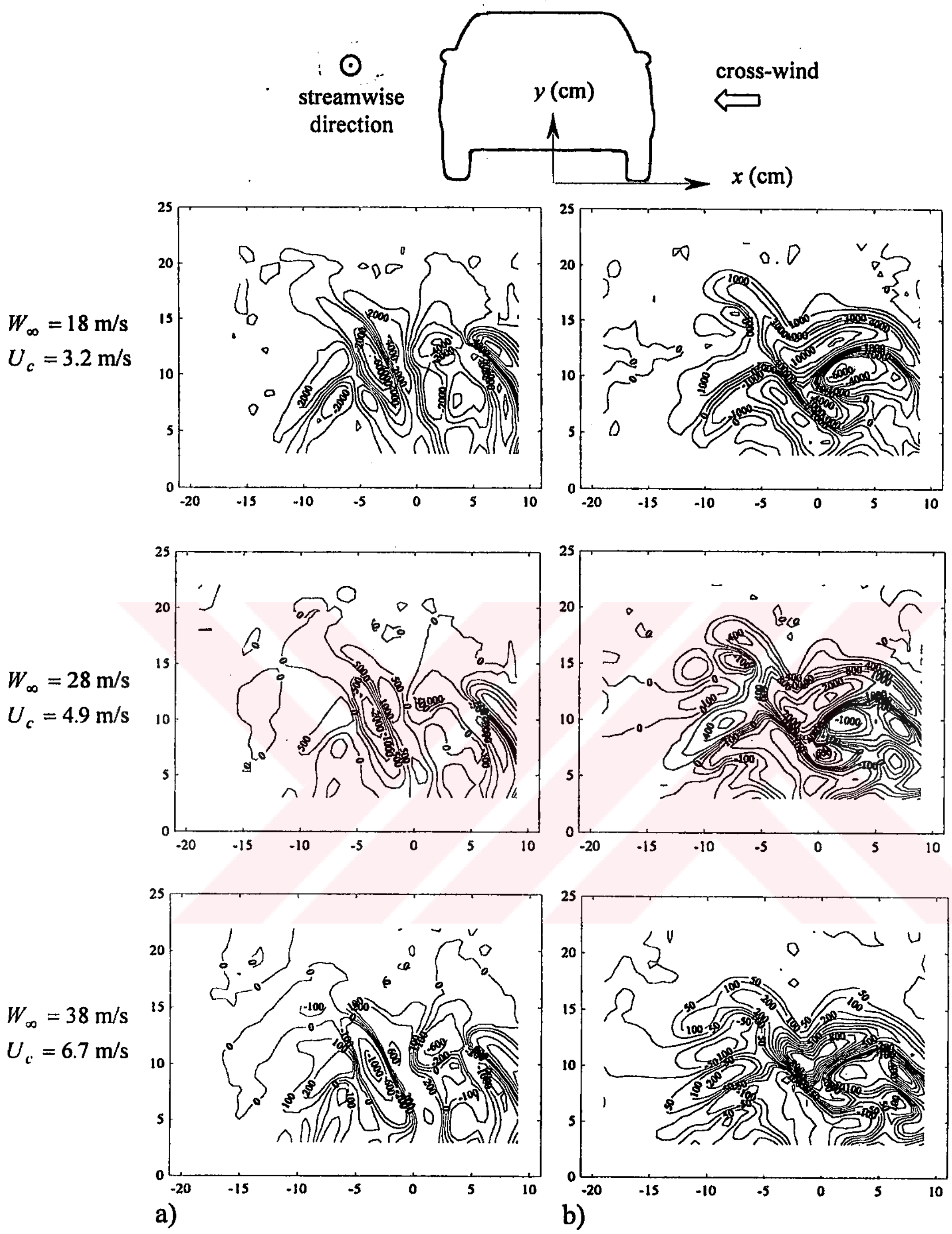

Figure 3.15 In-plane transport of streamwise component of turbulent kinetic energy;

$$\text{a) } -\frac{\partial}{\partial x}\left(\frac{1}{2}\overline{uw^2}\right)\left(\frac{L_F}{W_\infty^3}\right)\times 10^{10}, \text{ b) } -\frac{\partial}{\partial y}\left(\frac{1}{2}\overline{vw^2}\right)\left(\frac{L_F}{W_\infty^3}\right)\times 10^{10}.$$

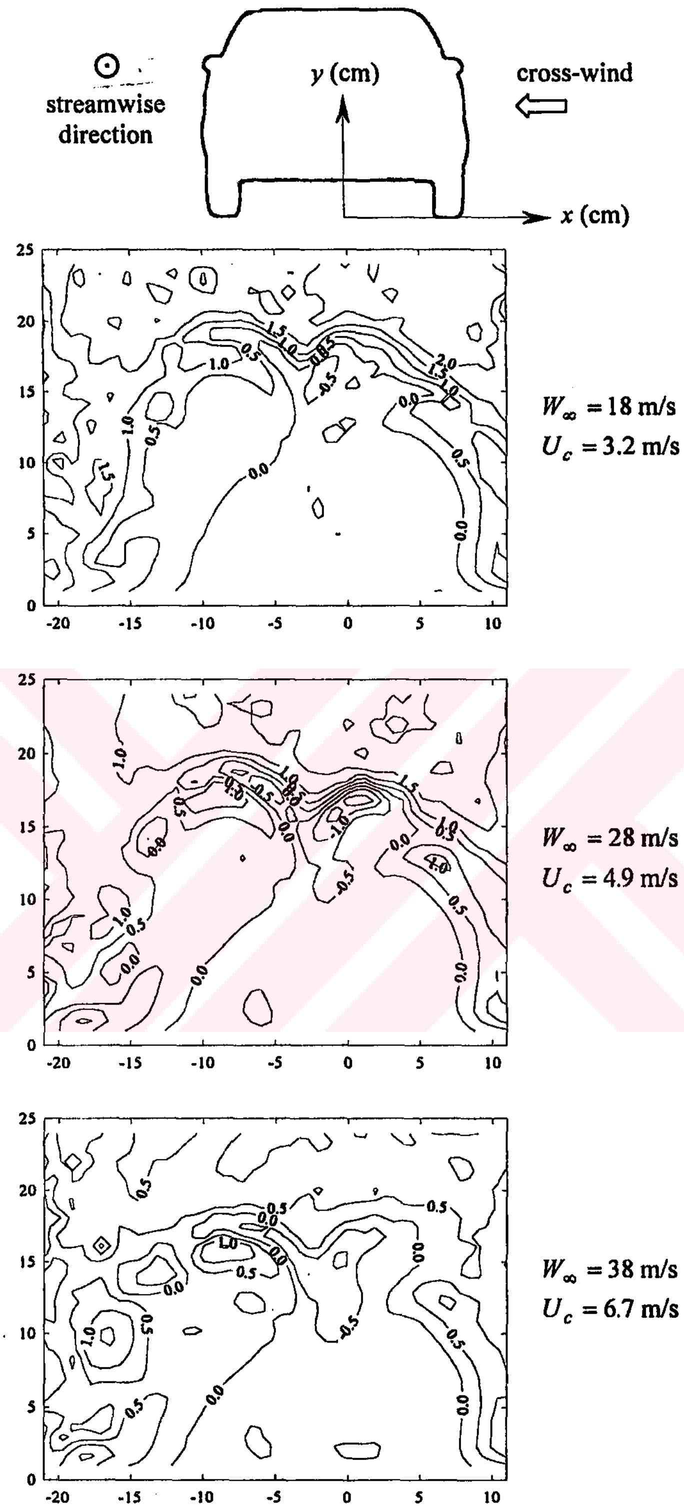

Figure 3.16 Triple-correlation between streamwise velocity and streamwise component of turbulent kinetic energy, $-\overline{ww^2}\Big/\left(\sqrt{\overline{w^2}}\right)^3$.

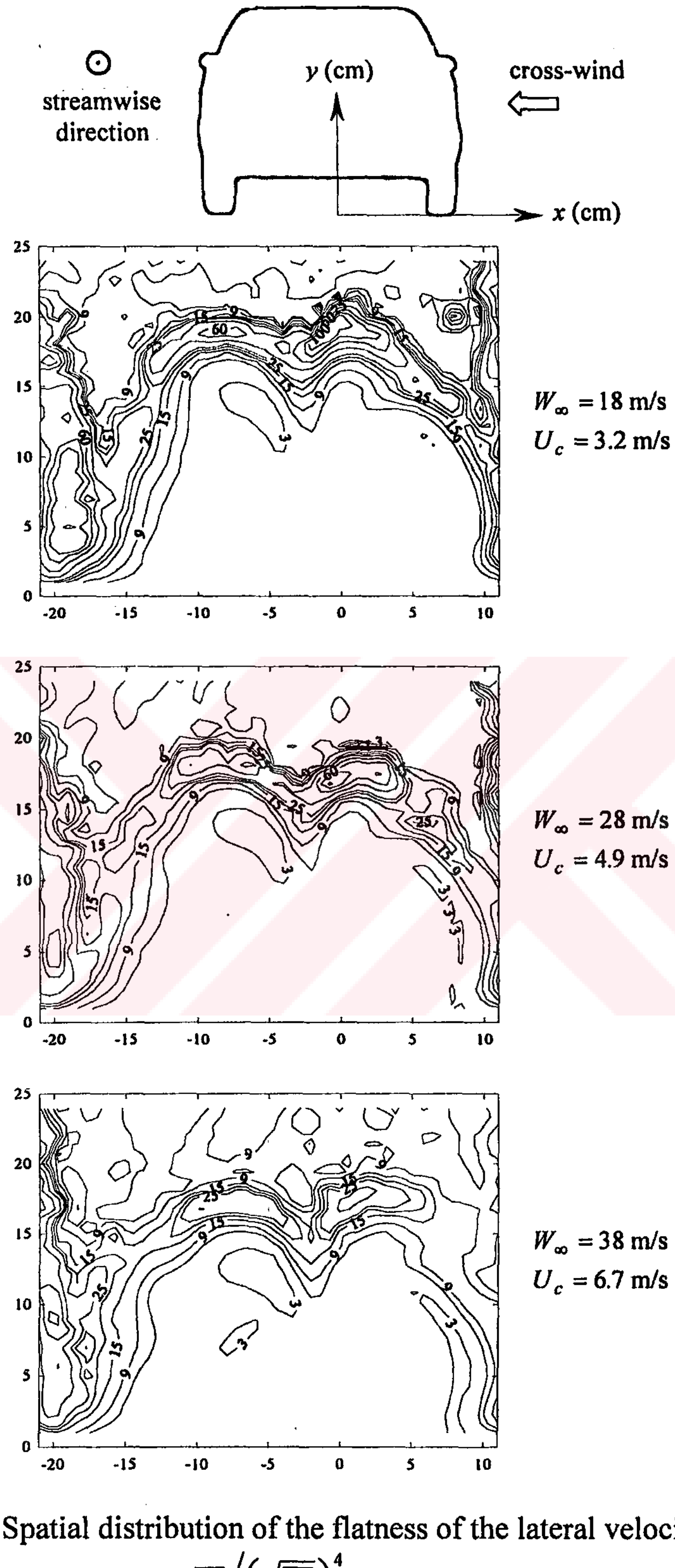

Figure 3.17 Spatial distribution of the flatness of the lateral velocity,

$$\overline{u^4}\Big/\left(\sqrt{\overline{u^2}}\right)^4 .$$

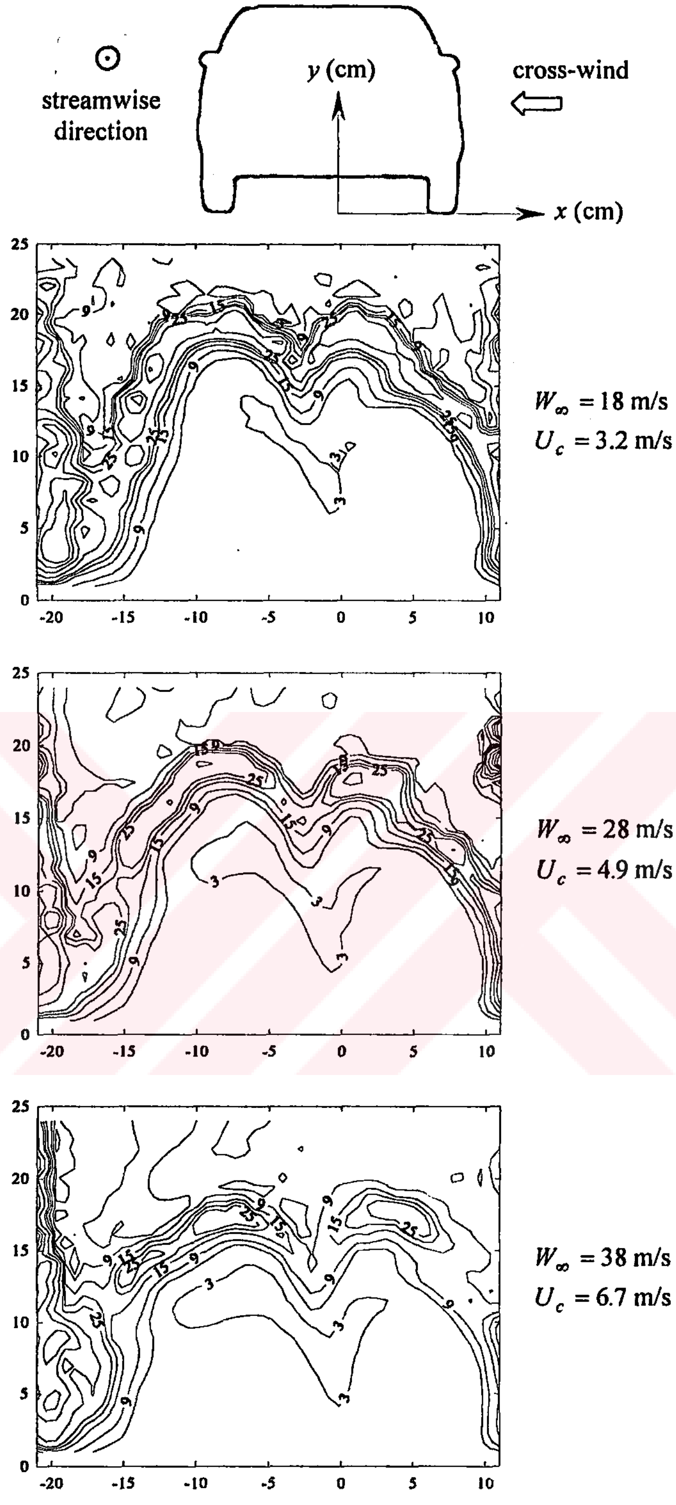

Figure 3.18 Spatial distribution of the flatness of the transversal velocity, $\overline{v^4}\Big/\left(\sqrt{\overline{v^2}}\right)^4$.

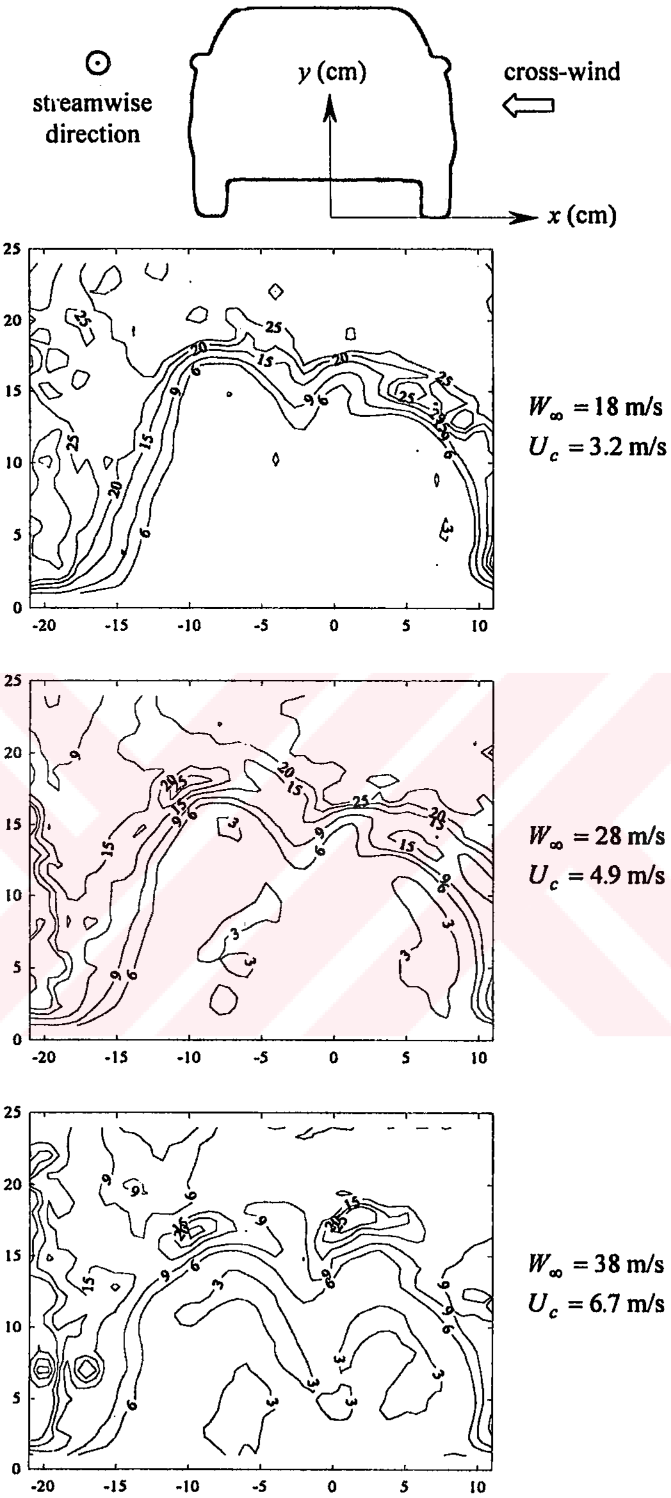

Figure 3.19 Spatial distribution of the flatness of the streamwise velocity, $\overline{w^4}\Big/\left(\sqrt{\overline{w^2}}\right)^4$.

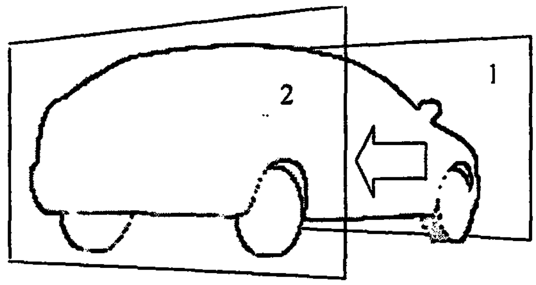

Figure 3.20 Surfaces through which streamwise flux calculated.

$$F_x = \frac{-\rho W_\infty U_c A_1 - \sum \rho \overline{W}\,\overline{U} \Delta x \Delta y}{\rho W_\infty^2 A_1} \tag{3.3}$$

$$F_y = \frac{-\sum \rho \overline{W}\,\overline{V} \Delta x \Delta y}{\rho W_\infty^2 A_1} \tag{3.4}$$

$$F_z = \frac{\rho W_\infty W_\infty A_1 - \sum \rho \overline{W}\,\overline{W} \Delta x \Delta y}{\rho W_\infty^2 A_1} \tag{3.5}$$

For the mean profiles presented in the previous section, these calculations were carried and the momentum flux deficits, non-dimensionalized by the momentum of the approaching flow for the three cases studied, are shown in figure 3.21. As it is evident from positive values of F_y and F_z, model is exposed to drag and lift forces while negative values of F_x indicate a side force in the direction of the crosswind. It is clear that when the approach velocity increases, the streamwise, transversal and lateral momentum deficits all decrease. The ratio F_y/F_z shows that the decrease in the lift force is sharper than the drag force. This puts in evidence that as the approach velocity increases, streamlines separated from the roof are not curved into the region immediately behind the car, but rather forms elongated wake pattern, the generating larger negative pressures behind the car, which increases drag but decreases lift. In addition, apart form the dynamic pressure imposed on the side surface of the car, which is only dependent on crosswind speed and the side surface of the car, there is a significant amount of side force applied on the car which decreases with the approach velocity even though the speed of the crosswind is constant.

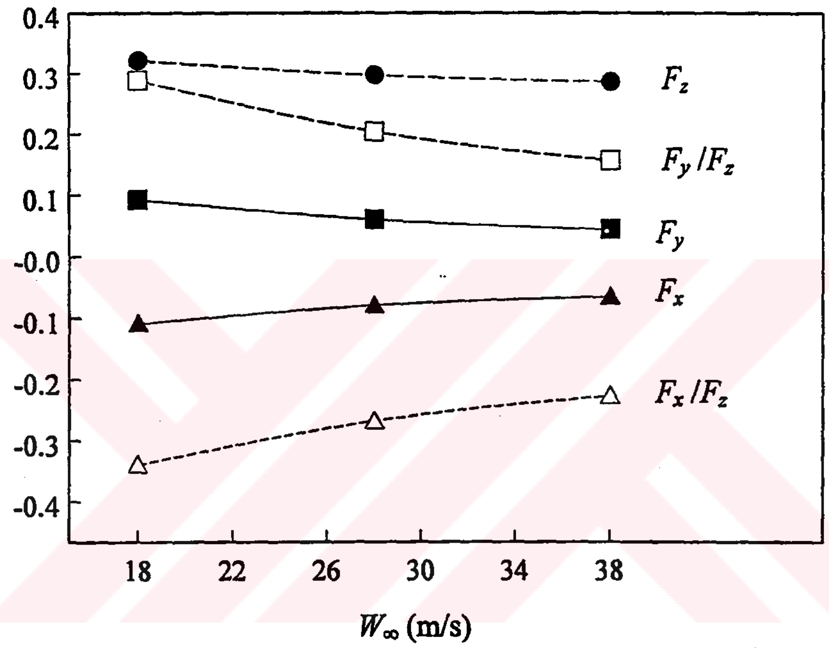

Figure 3.21 Streamwise flux of momentum in three directions

4. CONCLUSIONS

The turbulence characteristics of wake flow behind a three-dimensional car model exposed to a crosswind were investigated with emphasis on time-averaged mean and fluctuation velocities. The quantities related to forces applied on vehicle, as for example, streamwise vorticity and mechanisms of turbulence generation and transport were calculated with three different approach and crosswind speeds.

The results show that wake flow is mainly dominated by counter-rotating vortices, which extract considerable amount of kinetic energy from the mean flow via streamwise vorticity. This system, which governs the unsteady aerodynamics of the vehicle, seems less dependent on the driving speed. When there is crosswind, however, the vorticity was determined mainly by the in-plane velocities induced by the crosswind. Hence, the vortex system soaks the most of the energy put by the crosswind, which was then delivered back into the mean flow. The recycling of kinetic energy results in lesser turbulent dissipation and so lesser degradation of aerodynamic performance than expected.

This observation was also confirmed by the streamwise flux of lateral, transversal and streamwise momentum, which are the indication of steady aerodynamic loads applied on vehicles. Calculations of flux revealed that when the approach velocity is increased, the streamwise, transversal and lateral momentum deficits all decrease. This means that the vehicle becomes less sensitive to crosswinds. Furthermore, the decrease in the lift force was markedly higher than the other two. This was attributed to the fact that as the approach velocity increased, the shear layers separating from the model were stretched in the downstream direction, resulting in stagnation zone occurring further away from the car.

As a final remark, it should be noted that in this investigation changes in the approach velocity was in proportionate to the changes in crosswind speed, that is, the ratio of the two was constant. This leads to the conclusion that the vortex structure might depend on the ratio of the approach velocity to crosswind speed. This issue has considerable merit to be tested in future investigations.

REFERENCES

AHMED, S. R. 1981 An experimental study of the wake structures of typical automotive shapes, *J. Wind Engineering and Industrial Aerodynamics*, **61**, 49-62.

AKINS, R. E. and REINHOLD, T. A. 1998 Laser Doppler velocimeter measurements of separated shear layers on bluff bodies, *J. Wind Engineering and Industrial Aerodynamics*, **74-76**, 455-461.

ANGELIS, W., DRIKAKIS, D., DURST, F. and KHIER, W. 1996 Numerical and experimental study of flow over a two dimensional car model, *J. Wind Engineering and Industrial Aerodynamics*, **62**, 57-79.

BAKER, C. J. and HUMPHREYS, N. D. 1996 Assessment of the adequacy of various wind tunnel techniques to obtain aerodynamic data for ground vehicles in cross winds, *J. Wind Engineering and Industrial Aerodynamics*, **60**, 49-68.

BEARMAN, P. W. 1997 Near wake flows behind two- and three-dimensional bluff bodies, *J. Wind Engineering and Industrial Aerodynamics*, **69**, 33-54.

BROUGHTON, C. A. RAINBIRD, W. J. and KIND, R. J. 1995 An experimental investigation of interference effects for high blockage bluff bodies in a slotted-wall wind tunnel test section, *J. Wind Engineering and Industrial Aerodynamics*, **56**, 23-39.

BUCHHEIM, R., BEECK, M. A., HENTSCHEL, W., PIATEK, R. and SCHWABE, D. 1987 Advanced experimental techniques and their application to automotive aerodynamics, SAE Paper 870244, 21-36.

BRUUN, H.H. 1995 *Hot-Wire Anemometry; Principles and Signal Analysis*, Oxford Univ. Press, New York.

CIGADA, A., FALCO, M. and ZASSO, A. 2001 Development of new systems to measure the aerodynamic forces on section models in wind tunnel testing, *J. Wind Engineering and Industrial Aerodynamics*, **89**, 725-746.

DANTEC 1999 *Streamline; Installation and User's Guide Manual*, DANTEC Co.

DOMENICHINI, F., PEDRIZZETTI, G. and DE BERNARDINIS, B. 1997 A model for pressure distribution over obstacles due to separated flow, *J. Wind Engineering and Industrial Aerodynamics*, **66**, 51-67.

DOMINY, R. G. 1991 A technique for the investigation of transient aerodynamic forces on road vehicles in cross-winds, *Proc. IMECHE*, **205**, 173-181.

DOMINY, R. G. 1995 Flow unsteadiness over passenger vehicle rear surfaces, IMECHE Autotech Paper 95 C498/36/181.

DOMINY, R. G. and RYAN, A. 1999 An improved wind tunnel configuration for the investigation of aerodynamic cross-wind gust response, SAE Paper 1999-01-0808.

GARRY, K. P. 1996 Some effects of ground clearance and ground plane boundary layer thickness on the mean base pressure of a bluff vehicle type body, *J. Wind Engineering and Industrial Aerodynamics*, **62**, 1-10.

HAN, T. 1989 Computational analysis of three dimensional turbulent flow around a bluff body in ground proximity, *AIAA J.*, **27**, 1213-1219.

HANGAN, H. and VICKERY, B. J. 1997 A wake model for two-dimensional (sharp-edged) bluff bodies, *J. Wind Engineering and Industrial Aerodynamics*, **72**, 47-60.

HIMENO, R. and FUJTANI, K. 1993 Numerical analysis and visualization of flow in automotive aerodynamics development, *J. Wind Engineering and Industrial Aerodynamics*, **47**, 785-790.

HOWELL, J. P. 1996 The side load distribution on a Rover 800 saloon car under crosswind conditions, *J. Wind Engineering and Industrial Aerodynamics*, **60**, 139-153.

HOXEY, R. P., REYNOLDS, A. M., RICHARDSON, G. M., ROBERTSON, A. P. and SHORT J. L. 1998 Observation of Reynolds number sensitivity in the separated flow region on a bluff body, *J. Wind Engineering and Industrial Aerodynamics*, **73**, 231-249.

HUANG, R. F. and LIN, C. L. 2000 Velocity field of a bluff-body wake, *J. Wind Engineering and Industrial Aerodynamics*, **85**, 31-45.

KONG, L. and PARKINSON, G. V. 1995 Road vehicle model testing in a blockage tolerant wind tunnel, *J. Wind Engineering and Industrial Aerodynamics*, **57**, 137-143.

KOZAKA, E. O., ÖZKAN, G. and ÖZDEMİR İ. B. 2001 Wake structure of a three dimensional car model, to be submitted to *J. Wind Engineering and Industrial Aerodynamics*.

MOKRY, M. 1995 Wall interference correction to drag measurements in automotive wind tunnels, *J. Wind Engineering and Industrial Aerodynamics*, **56**, 107-122.

ÖZDEMİR, İ.B., 2001 *Introduction to Mechanics of Turbulence*, Course Notes, İTÜ Institute of Science and Technology.

PARAMESWARAN, S., KIRIS, I., SUN, R. and GLEASON, M. 1993 Flow structure around a 3D bluff body in ground proximity: A computational study, *J. Wind Engineering and Industrial Aerodynamics*, **46**, 791-800.

PARAMESWARAN, S, ANDRA, R., SUN, R. and GLEASON, M. 1997 A critical study on the influence of far field boundary conditions on the pressure distribution around a bluff body, *J. Wind Engineering and Industrial Aerodynamics*, **67-68**, 117-127.

RYAN, A. and DOMINY, R. G. 1997 The transient aerodynamic characteristics of a passanger vehicle passing through a cross-wind jet, IMECHE Autotech Paper 97.

RYAN, A. and DOMINY, R. G. 1998 The aerodynamic forces induced on a passenger vehicle in response to a transient cross-wind gust at a relative incidence of 30 degrees, SAE Paper 980392.

SIMS-WILLIAMS, D. B. and DOMINY, R. G. 1998 Experimental investigation into unsteadiness and instability in passenger car aerodynamics, SAE Paper 980391.

WILLIAMSON, C. H. K. 1997 Advances in our understanding of vortex dynamics in bluff body wakes, *J. Wind Engineering and Industrial Aerodynamics*, **69-71**, 3-32.

WOLF, T. 1995 Design of a variable contraction for a full-scale automotive wind tunnel, *J. Wind Engineering and Industrial Aerodynamics*, **56**, 1-21.

TENNEKES, H. and LUMLEY, J.L., 1972 *A First Course in Turbulence*, Cambridge, MIT Press.

TOWNSEND, A.A., 1976. *The Structure of Turbulent Shear Flow*, Second Edition, Cambridge University Press, Cambridge.

BIOGRAPHY

Esra Özdemir was born in 1974 in Isparta where she completed her primary, secondary and high school educations. She graduated from the Department of Chemistry at the Science Faculty of Ege University with B.A. Chem. degree in 1997. Since 1998, she has been a graduate student at the Defense Technologies Program Energy Division at the Institute of Science and Technology, İTU. Between 1998 and 1999, she was involved in a research on laser diagnostics at the Institut für Technishe Mechanik at the RWTH Aachen.

Beginning with summer 2000, she joined into the Fluids Laboratories of the Mechanics Division of the School of Mechanical Engineering as a research student with a scholarship from TÜBİTAK under grant MİSAG-163.

Since 1998, she has been married with one son.